



# Caltech lab experiments and the insights they provide into solar corona phenomena

Paul M. Bellan

Department of Applied Physics and Materials Science, California Institute of Technology, Pasadena CA 91125

---

P. M. Bellan, MC 128-95, California Institute of Technology, Pasadena CA 91125. (pbel-  
lan@caltech.edu)

This article has been accepted for publication and undergone full peer review but has not been through the copyediting, typesetting, pagination and proofreading process which may lead to differences between this version and the Version of Record. Please cite this article as doi: 10.1029/2020JA028139

**Abstract.** A comprehensive overview of two decades of Caltech experiments relevant to solar corona physics is presented. The extent to which the experiments scale to the solar corona, the basic configurations and operation, and the importance of the magnetic force  $\mathbf{J} \times \mathbf{B}$  common to all the experiments is discussed. Summaries are given of the various configurations used, the main observations, and interpretations of these observations, including new models developed to provide these interpretations. Topics include observations and explanations for flux rope self-collimation, axial flows along flux ropes, eruption of arched flux ropes, strapping magnetic fields that inhibit eruption, the torus instability, and effects such as X-ray emission of a kink-driven secondary Rayleigh-Taylor instability.

## 1. Introduction

### 1.1. History and Motivation

Laboratory experiments on phenomena relevant to the solar corona began at Caltech in the mid 1990's. These experiments, an outgrowth of ongoing spheromak experiments, exploited the realization that spheromak physics is closely related to solar corona physics as both involve non-equilibrium magnetohydrodynamics (MHD), injection of magnetic helicity, and relaxation to minimum-energy states. Initial experiments had minimal diagnostics and there was little understanding of how results could be scaled to the solar corona. With time, the experiments and diagnostics became more sophisticated, the scalability to the solar corona was understood, and models motivated by the experiment were developed and applied to the experiment and to the solar corona.

### 1.2. Benefits of experiments

The traditional methods for studying the solar corona are observation, analytic models, and numerical models. Laboratory experiments provide a different and complementary approach. Unlike solar observations, laboratory experiments are repeatable with control of both initial and boundary conditions. Repeatability allows for scanning a single parameter to determine the dependence on that parameter. In contrast, the solar corona is neither repeatable nor controllable so statistical methods must be used to determine parametric relationships. Analytic and numerical models necessarily involve simplifying assumptions so significant physics is omitted. For example, analytic models typically focus on a small subset of the entire system by making restrictive assumptions about geometry, space scale, or time scale. While numerical models can characterize more complex geometry,

numerical models have limited ability to characterize multi-scale physics. By virtue of being real, laboratory experiments automatically involve no assumptions about physics, automatically involve realistic geometry, and automatically contain multi-scale physics. However, care is required in relating laboratory experiments to the solar corona because some aspects of the experiments scale well to the solar corona whereas others do not. The features that do not scale well are not necessarily irrelevant because consideration of these features stimulates understanding of how non-scalable but related phenomena might occur in the solar corona. Experiments often provide discovery of unexpected new phenomena and these discoveries motivate development of new models that can then be immediately validated by further experiments.

## 2. Scalability to the Solar Corona

Because the ideal MHD equations have no intrinsic scale, laboratory experiments are relevant to the solar corona despite the approximately five to eight orders of magnitude difference between time and length scales (microseconds and centimeters in the laboratory versus minutes and megameters for the solar corona). A general method for scaling laboratory experiments to solar or even astrophysical situations was developed by *Ryutov et al.* [2000, 2001] who showed that two ideal MHD plasmas can be *directly* scaled to each other if they have the same reference  $\beta_0 = \mu_0 P_0 / B_0^2$ . Here  $P_0 = n_0 \kappa T_0$  and quantities with subscript zero are reference values used for normalization. Scalability results because when the ideal MHD equations are expressed in dimensionless form, the only remaining parameter is  $\beta_0$ . Thus, for *any* reference mass density  $\rho_0$ , reference length  $l_0$ , and reference length  $B_0$  *all* ideal MHD plasmas having the same  $\beta_0$  are governed by a unique set of

dimensionless equations, namely:

$$\bar{\rho} \left( \frac{\partial \bar{\mathbf{U}}}{\partial \bar{t}} + \bar{\mathbf{U}} \cdot \bar{\nabla} \bar{\mathbf{U}} \right) = (\bar{\nabla} \times \bar{\mathbf{B}}) \times \bar{\mathbf{B}} - \beta_0 \bar{\nabla} \bar{P} \quad (1a)$$

$$\frac{\partial \bar{\mathbf{B}}}{\partial \bar{t}} = \bar{\nabla} \times (\bar{\mathbf{U}} \times \bar{\mathbf{B}}) \quad (1b)$$

$$\frac{\partial \bar{\rho}}{\partial \bar{t}} + \bar{\nabla} \cdot (\bar{\rho} \bar{\mathbf{U}}) = 0 \quad (1c)$$

$$\left( \frac{\partial}{\partial \bar{t}} + \bar{\mathbf{U}} \cdot \bar{\nabla} \right) (\bar{P} \bar{\rho}^{-\gamma}) = 0 \quad (1d)$$

where

$$\begin{aligned} v_{A0} &= \frac{B_0}{\sqrt{\mu_0 \rho_0}} \\ \tau_{A0} &= \frac{l_0}{v_{A0}} \\ \bar{\mathbf{x}} &= \frac{\mathbf{x}}{l_0} \\ \bar{t} &= \frac{t}{\tau_{A0}} \\ \bar{\nabla} &= l_0 \nabla \\ \bar{\rho} &= \frac{\rho}{\rho_0} \\ \bar{\mathbf{B}} &= \frac{\mathbf{B}}{B_0} \\ \bar{\mathbf{U}} &= \frac{\mathbf{U}}{v_{A0}} \\ \bar{P} &= \frac{P}{P_0}. \end{aligned} \quad (2)$$

The crux of Ryutov's scaling method involves defining three parameters  $c_1 = l_{0lab}/l_{0solar}$ ,  $c_2 = \rho_{0lab}/\rho_{0solar}$ , and  $c_3 = P_{0lab}/P_{0solar}$  which then give the scaling from laboratory plasma to solar plasma parameters as

$$B_{solar} = \frac{B_{lab}}{\sqrt{c_3}}, \quad v_{A,solar} = v_{A,lab} \sqrt{\frac{c_2}{c_3}}, \quad \tau_{solar} = \frac{\tau_{lab}}{c_1} \sqrt{\frac{c_3}{c_2}}. \quad (3)$$

Equation 3 shows that laboratory plasmas are scale models of solar plasmas to the extent that both are described by Eqs.1(a-d). Table 1 lists reference and scaled quantities for a typical Caltech argon  $\beta_0 = 10^{-2}$  laboratory plasma and two solar situations, namely  $\beta_0 = 10^{-2}$  corona and  $\beta_0 = 10^{-2}$  chromosphere. Table 1 shows that Eqs.1(a-d) describe the *same* dimensionless space-time evolution for (i) an event lasting 15  $\mu$ s in a 2 eV argon laboratory plasma having reference density  $3 \times 10^{16} \text{ cm}^{-3}$  and reference magnetic field 10 kG and (ii) a morphologically similar solar corona event lasting 19 seconds having  $T_0 = 90 \text{ eV}$ , reference density  $10^{10} \text{ cm}^{-3}$  and reference magnetic field 40 G. Stating that the reference density is  $10^{10} \text{ cm}^{-3}$  does not mean that the density has this value at all times or locations but rather means that  $10^{10} \text{ cm}^{-3}$  is a convenient unit in which to measure density so the actual density ranges from some fraction of this density (e.g., 1/4) to some multiple of this density (e.g., 4 $\times$ ). To make the laboratory plasma act as a scale model of the solar situation, the dimensionless initial and boundary conditions must be the same; a numerical MHD solution of Eqs.1(a-d) then gives identical results for the laboratory and solar plasmas.

This discussion shows that laboratory experiments can be scaled to the solar corona to the extent that both the experiments and the solar corona are characterized by ideal MHD. However, many phenomena exist beyond the scope of ideal MHD and these phenomena are in general not directly scalable. Nevertheless, the experiments provide useful insights regarding many of these non-MHD phenomena and these insights can be applied to the solar corona even if direct scaling is not possible (this will be discussed in Sections 4.9 and 4.12).

### 3. Plan of the paper, diagnostics, and types of configuration

To keep this paper within length requirements, it will be restricted to a qualitative overview of the main experimental results and their physical interpretation. Reference will be given to the original papers where experimental results and analysis are presented; a detailed and extensive discussion is also available in *Bellan* [2018c]. The experiments used a wide range of diagnostics including: high speed movies of both visible and extreme ultraviolet (EUV) radiation, stereo imaging, three-dimensional volumetric measurement of the time-dependent magnetic field vector, electric current measurement, voltage measurement, X-ray emission, emission of various plasma waves, spectroscopic measurements of density via Stark broadening, temperature and bulk motion via Doppler broadening/shift, magnetic field via Zeeman splitting, density via laser interferometry, density and electron temperature via Thomson scattering. Two types of geometries have been used, the first will be called bipolar and the second coaxial. The bipolar geometry has the topology of a single coronal loop. The coaxial geometry has eight initial interacting loops similar to the legs of a spider with the eight loops merging to form a coaxial jet. Plasma parameters for both configurations are in the range  $n \sim 10^{21} - 10^{23} \text{ m}^{-3}$ ,  $B \sim 0.05 - 0.5 \text{ T}$ ,  $I \sim 50 - 150 \text{ kA}$ ,  $T \sim 2 - 3 \text{ eV}$ , radius  $\sim 2 - 5 \text{ cm}$ , length  $\sim 5 - 50 \text{ cm}$  and the time interval between shots is 2 minutes. Shot-to-shot reproducibility is 3-10% depending on operating regime and what is being measured. In the rest of this chapter, the direction *axial* will refer to the direction going from one electrode to the other and the direction *azimuthal* will refer to the direction of the magnetic field associated with an axial current. There is thus an axial magnetic field and an axial current with the axial current making an azimuthal

magnetic field that links the axial magnetic field. This linking corresponds to there being magnetic helicity and to the total magnetic field being twisted or helical.

### 3.1. Bipolar geometry and operation

Figure 1 sketches the basic experimental sequence used to create laboratory plasmas having shape and dynamics similar to solar corona loops [*Hansen and Bellan, 2001; Sten-son and Bellan, 2008, 2012*] while Fig.2 shows the actual electrode configuration and photographs of typical plasmas. First, an electromagnet [Fig. 1(a)] produces an initial quasi-static (5 ms time scale), arch-shaped potential magnetic field with a 10-20 cm characteristic length. The much larger vacuum chamber dimension means that the plasma is unaffected by the vacuum chamber side walls and so behaves as if in semi-infinite space. After the potential magnetic field has been established, high-speed electromagnetically pulsed gas valves briefly puff a neutral gas cloud into the region between the magnet poles. The amount of injected gas is arranged to enable breakdown in the next step of the sequence where a high-energy capacitor bank charged to several kilovolts is connected by a high-speed electronic switch across the magnet poles [Fig. 1(b)]. The high voltage breaks down the neutral gas in about  $0.1 \mu\text{s}$  to form a low-density plasma [Fig. 1(b)]. The electric current flowing through the tenuous plasma produced at breakdown is small and follows the arched vacuum field lines. This current then ramps up and by  $5\text{-}7 \mu\text{s}$  has attained several 10's of kA. The MHD force associated with this large electric current drives fast upflowing plasma jets from both footpoints [Fig. 1(b)]. These upflowing plasma jets quickly collide at the apex of the arched loop and fill the flux tube with plasma. The flux tube collimates [Fig. 1(c)] as the two jets collide. All the while, the magnetic hoop force

causes an expansion of the arch major radius [Fig. 1(d)]. A dip is often observed at the apex and, in certain situations, a kinetic jet appears at the loop apex [Fig. 1(d)].

The sequence shown in Fig. 1 occurs only if neutral gas is injected. The jet upflows from the footpoints shown in Fig. 1(b) are predicted in *Bellan* [2003], have been modeled numerically by *Zhai et al.* [2014], and recently the force driving these flows has been measured by *Haw and Bellan* [2017]. The jet upflows were demonstrated by *Stenson and Bellan* [2008, 2012] who injected different gases at the two footpoints so that injected gas could be clearly associated with its originating footpoint. Blueshifts associated with the upflows have been measured by *Tripathi et al.* [2007].

### 3.2. Coaxial geometry and operation

The coaxial magnetized plasma source is similar but has coaxial symmetry and consists of a copper disk surrounded by a concentric co-planar copper annulus. The coaxial source has a coil located behind the gap between the disk and the annulus; this coil provides a bias poloidal magnetic flux linking the disk to annulus (poloidal refers to the  $r$ - $z$  plane in a cylindrical coordinate system). The sequence of operation is similar to the solar loop plasma and is as follows. First, an external coil is energized to produce a 1-2 mWb poloidal magnetic flux linking the inner copper disk to the outer copper annulus. Next, gas (H, Ar, N, Ne, Kr, or Xe) is puffed through eight orifices on the disk and eight on the annulus. Then a several kilovolt potential drop is applied across the gap separating disk from annulus. The high voltage breaks down the injected gas to form eight arched, plasma-filled flux tubes (“spider legs”) linking the disk to the annulus as in the 4  $\mu$ s image of Fig.3. Each spider leg is similar to a solar loop plasma and electric current driven by the applied voltage flows along each spider leg. Since the spider legs carry

parallel currents, their inner segments mutually attract and merge [4.5 to 6  $\mu\text{s}$  in Fig. 3] to form a central column jet [6  $\mu\text{s}$  in Fig.3] which lengthens (6.5 to 10  $\mu\text{s}$ ) and then becomes kink unstable [10  $\mu\text{s}$  in Fig.3]. This merging requires a magnetic reconnection because the merged spider legs wrap around each other so the magnetic topology has changed from separated distinct spider legs to spider legs wrapped around a common axis. *Zhai* [2015] imaged this wrapping by injecting nitrogen from inner nozzles 1-4 and argon from inner nozzles 5-8 and then used filters in front of the camera to distinguish argon from nitrogen. After the spider legs have merged, the lengthening jet behaves in a manner consistent with ideal MHD, i.e., consistent with the assumption that the electric field vanishes in the frame moving with the jet. Having  $\mathbf{E} = 0$  in the jet frame is an essential property of a numerical simulation of the jet experiment [*Zhai et al.*, 2014] and of an analytic model of the lengthening jet [*Bellan*, 2020].

### 3.3. Importance and characterization of the $\mathbf{J} \times \mathbf{B}$ magnetic force

The MHD equation of motion, Eq.1a, prescribes the motion of a plasma subjected to the combined  $\mathbf{J} \times \mathbf{B}$  and hydrodynamic  $-\nabla P$  forces. The MHD induction equation, Eq.1b, simultaneously prescribes the constraint that magnetic flux is frozen into the frame of the moving plasma. The experiments reveal the importance of the current density  $\mathbf{J}(\mathbf{x}, t)$ . Until recently,  $\mathbf{J} \times \mathbf{B}$  forces have been generally ignored in solar corona models where attention has instead focused on magnetic field line motion as the prime agent governing solar corona behavior [*Parker*, 1996, 2007]; often the magnetic field is assumed to be potential (i.e.,  $\mathbf{B} = \nabla\chi$  so  $\mathbf{J} = \mu_0^{-1}\nabla \times \mathbf{B} = 0$ ) or force-free so  $\mathbf{J} \times \mathbf{B} = 0$ . However, in a low  $\beta$  plasma such as the solar corona, it is clearly important to understand implications of the  $\mathbf{J} \times \mathbf{B}$  force because it is this force that drives the plasma motion. Most obviously,

the  $\mathbf{J} \times \mathbf{B}$  force is finite only where  $\mathbf{J}$  is finite which is the case only when the magnetic field is non-potential and  $\mathbf{J}$  is not parallel to  $\mathbf{B}$ . On the other hand,  $\mathbf{B}$  is finite nearly everywhere as magnetic field nulls are points in three-dimensional space and so have infinitesimal volume [Greene, 1988], i.e., are of measure zero. Because forces can exist only if  $\mathbf{J}$  is finite, it is reasonable to consider  $\mathbf{J}$  to be the prime agent governing dynamical behavior. The special case where  $\mathbf{J}$  is finite but parallel to  $\mathbf{B}$  so as to give force-free equilibria cannot exist when dynamical behavior (e.g., eruption) occurs because a force is required to accelerate both the plasma and its embedded magnetic field away from equilibrium in order to have dynamics.

Numerous situations have been proposed where the  $\mathbf{J} \times \mathbf{B}$  force drives important dynamics [Melrose, 1995; Khodachenko et al., 2003; Chen, 2003; Kliem and Torok, 2006] and these situations cannot be described by potential or force-free models nor by models restricted to describing the motion of magnetic field lines. Controversy has existed regarding whether the electric current and magnetic forces are important. A point of view that the electric current and resulting magnetic forces are neither fundamental nor important has been advocated by Parker [1996, 2001, 2007] who asserted that the magnetic field rather than the electric current is fundamental and objected to the electric current point of view invoked here and previously by Alfvén and Carlqvist [1967]; Alfvén [1986]; Melrose [1995]. In the author's opinion this dispute is analogous to arguing in mechanics whether acceleration or velocity is the more fundamental quantity, i.e., the 'prime mover'; arguing that magnetic field is the prime mover is like arguing that velocity is the prime mover driving acceleration. The question of whether current is a cause or an effect was discussed in Bellan [2003] where it was shown that, in the context of a flux rope intercepting a

surface with prescribed boundary conditions, the axial component of the current can be considered to be a cause whereas the azimuthal component of the current can be considered to be an effect. This is because the axial component of the current is determined by the boundary condition imposed at the surface being intercepted (electrode in experiment, solar surface on sun) whereas the azimuthal component of the current does not intercept a surface and so is instead determined by the extent to which the axial magnetic field is either compressed or rarefied as a result of the competition between the pinch force, the internal pressure, and the external pressure. In the experiments the axial component of the current comes from electrodes and is dictated by the power supply while on the sun the axial component of the current comes from some undetermined source that exists beneath the solar surface. The azimuthal component of the current is a consequence of the axial magnetic field lines being squeezed together by the pinch force associated with the axial current (paramagnetism) or being spread apart as a result of the internal pressure (diamagnetism); this competition between paramagnetism and diamagnetism has been discussed in the tokamak context by *Li and Cross* [1994]. The MHD Ohm's law expressed as  $\mathbf{E} + \mathbf{U} \times \mathbf{B} = \eta \mathbf{J}$  is agnostic about the value of current density  $\mathbf{J}$  in the limit that  $\eta \rightarrow 0$ , i.e., in the ideal limit. Thus, for any given finite current density  $\mathbf{J}$ ,  $\eta$  can be considered to be so small that  $|\eta \mathbf{J}| \ll |\mathbf{E}|$  and  $|\eta \mathbf{J}| \ll |\mathbf{U} \times \mathbf{B}|$  so the Ohm's law can be considered to be  $\mathbf{E} + \mathbf{U} \times \mathbf{B} = 0$ . However, as will be shown in Sec.4.9 when the spatial gradient scale becomes so small as to be of the order of the ion skin depth  $d_i = c/\omega_{pi}$  then the Ohm's law is no longer given by ideal MHD and changes to a form that depends on  $\mathbf{J}$  via Hall terms.

The  $\mathbf{J} \times \mathbf{B}$  force can be characterized in several equivalent ways. These characterizations provide an intuitive sense for how a system will evolve without having to go to the effort of constructing a detailed solution to the nonlinear system of equations. One required feature of any characterization is that it must not imply the existence of a force along the magnetic field since clearly  $\mathbf{J} \times \mathbf{B} \cdot \mathbf{B} = 0$ ; thus the commonly used concept of field line “tension” cannot be correct because a tension would be a force along a field line. Three useful characterizations of the  $\mathbf{J} \times \mathbf{B}$  force are provided below and will be referred to in the rest of this chapter. In the author’s opinion these are respectively the simplest, the most accurate, and the most profound characterizations.

The *simplest* way to characterize the  $\mathbf{J} \times \mathbf{B}$  force is the statement that *parallel currents mutually attract whereas anti-parallel currents mutually repel*. Mutual attraction between parallel currents is the basis of the pinch force that provides confinement of finite pressure plasmas. Mutual repulsion between anti-parallel currents provides the hoop force that drives the kink instability [Hsu and Bellan, 2003], the expansion of the major radius of an arched flux rope [Chen et al., 2006; Stenson and Bellan, 2012], the torus instability [Kliem and Torok, 2006], and magnetically driven jets [Kumar and Bellan, 2009; Bellan, 2018a, b].

The *most accurate* way of characterizing the magnetic force is to use the vector identity  $\nabla B^2/2 = \mathbf{B} \cdot \nabla \mathbf{B} + \mathbf{B} \times \nabla \times \mathbf{B}$  together with Ampere’s law  $\nabla \times \mathbf{B} = \mu_0 \mathbf{J}$  to express the

magnetic force as

$$\begin{aligned}
 \mathbf{J} \times \mathbf{B} &= \frac{1}{\mu_0} (\nabla \times \mathbf{B}) \times \mathbf{B} \\
 &= -\nabla \left( \frac{B^2}{2\mu_0} \right) + \frac{1}{\mu_0} B \hat{B} \cdot \nabla (B \hat{B}) \\
 &= -\nabla \left( \frac{B^2}{2\mu_0} \right) + \frac{1}{\mu_0} (B \hat{B} \cdot \nabla B) \hat{B} + \frac{1}{\mu_0} B^2 \hat{B} \cdot \nabla \hat{B}
 \end{aligned} \tag{4}$$

so

$$\mathbf{J} \times \mathbf{B} = -\nabla_{\perp} \left( \frac{B^2}{2\mu_0} \right) + \frac{1}{\mu_0} \kappa B^2. \tag{5}$$

Here

$$\nabla_{\perp} = \nabla - \hat{B} (\hat{B} \cdot \nabla) \tag{6}$$

is the gradient in the direction perpendicular to the magnetic field and

$$\kappa = \hat{B} \cdot \nabla \hat{B} = -\frac{\hat{R}}{R} \tag{7}$$

characterizes field curvature where  $R$  is the local radius of curvature of the magnetic field and  $\hat{R}$  is a unit vector pointing out from the center of curvature along the radius of curvature.

The first term on the RHS of Eq.5 (i.e., term involving  $\nabla_{\perp}$ ) is called the magnetic pressure term; the second term (term involving  $\kappa$ ) is called the magnetic curvature term. Both these terms are perpendicular to  $\mathbf{B}$  so both provide no forces along the magnetic field [to see that the curvature term is perpendicular note that  $\frac{1}{2}\nabla (\hat{B} \cdot \hat{B}) = 0 = \hat{B} \cdot \nabla \hat{B} + \hat{B} \times \nabla \times \hat{B}$ ]. If the magnetic field is potential (i.e.,  $\mathbf{J} = 0$ ) then the LHS of Eq.5 vanishes so the two RHS terms must be equal in magnitude and opposite in sign showing that it can be dangerous and misleading to try to explain magnetic forces using just one of these RHS terms. If the magnetic field is force-free (i.e.,  $\mathbf{J}$  is finite, but parallel to  $\mathbf{B}$ ) the two terms on the RHS of Eq.5 again cancel. Finally, there is the possibility that one or the other of

the two terms on the RHS of Eq.5 dominates. If the magnetic pressure term dominates, then the magnetic pressure force pushes plasma from regions of large magnetic field to regions of small magnetic field, but only in a direction perpendicular to the magnetic field. If the magnetic curvature term dominates, then the magnetic force pushes the plasma in a direction required to straighten out the curvature. This straightening of curvature is analogous to the consequence of a tension force on a plucked guitar string so the effect of the curvature force is partially like the effect of a tension force. However, in contrast to guitar string tension, the magnetic curvature force only acts to straighten out magnetic field curvature and does not act to contract the length of a magnetic field line (i.e., there is no force parallel to  $\mathbf{B}$ ).

The balance between magnetic curvature and magnetic pressure forces can be intricate. An important example is the situation of a uniform, finite-radius axial current  $I$  as in a wire. If the current radius is given by  $a$  so  $J_z = I/(\pi a^2)$  for  $r < a$  and  $J_z = 0$  for  $r > a$ , then from Ampere's law the associated azimuthal magnetic field is  $B_\phi = \mu_0 I r / (2\pi a^2)$  for  $r < a$  and  $B_\phi = \mu_0 I / (2\pi r)$  for  $r > a$ . For  $r < a$ , the magnetic pressure force is thus  $-(2\mu_0)^{-1} \nabla_\perp B^2 = -I^2 r \hat{r} / (4\pi^2 \mu_0 a^4)$  while the magnetic curvature force is  $\kappa B^2 / \mu_0 = -I^2 r \hat{r} / (4\pi^2 \mu_0 a^4)$  so here the magnetic pressure and magnetic curvature forces are identical and add to give a net inward force  $\mathbf{J} \times \mathbf{B} = -I^2 r \hat{r} / (2\pi^2 \mu_0 a^4)$ . This is the pinch force that in equilibrium balances an outward force due to  $-\nabla_\perp P$  and so provides plasma confinement. However, for  $r > a$ , the magnetic pressure force is  $-(2\mu_0)^{-1} \nabla_\perp B^2 = I^2 \hat{r} / (4\pi^2 \mu_0 r^3)$  while the magnetic curvature force is  $\kappa B^2 / \mu_0 = -I^2 \hat{r} / (4\pi^2 \mu_0 r^3)$  so the magnetic pressure and magnetic curvature forces, being equal and opposite, cancel to give no net force. The magnetic pressure force is closely related to the mutual repulsion

between anti-parallel currents since a magnetic field maximum exists between anti-parallel currents; an example is the ‘hoop force’ where oppositely directed currents on the opposite sides of a current loop mutually repel and act to increase the loop major radius.

The *most profound* way of characterizing the MHD force is based on consideration of the energy stored in the entire volume  $V$  of magnetic field for given, fixed boundary conditions. This consideration is based on a variational argument (see p. 306-309 of *Bellan* [2006]) which shows that of all the possible magnetic fields satisfying a given boundary condition, the potential field is the one having the lowest total magnetic energy  $W = (2\mu_0)^{-1} \int_V B^2 d^3r$ . Furthermore, this consideration shows that force-free fields are local minima of  $W$ . This is analogous to the energy structure of an atom where the potential magnetic field corresponds to the ground state and force-free magnetic fields correspond to higher-energy stable quantum states. An arched flux rope is non-potential to the extent that it is twisted since twist corresponds to the existence of current. A large axial current will give a large upwards  $\nabla_{\perp} B^2$  force which is in the direction to cause eruption since the magnetic field is stronger on the concave side of the arch than on the convex side (e.g., consider electric current flowing from the left footpoint to the right footpoint in Fig.1 and in the photos in Fig. 2). However, the force associated with curvature of the axial magnetic field opposes eruption so the axial electric current has to be sufficiently large for its upwards  $\nabla_{\perp} B^2$  force to overwhelm the downward-directed magnetic curvature force associated with the axial magnetic field. The situation is analogous to blowing up a balloon where the magnetic pressure force corresponds to the pressure in the balloon trying to make the balloon radius larger and the magnetic

curvature force corresponds to the stretching of the balloon skin which is trying to make the balloon radius smaller.

The induction equation Eq.1b has the property of freezing magnetic flux into the frame of the moving plasma (see derivation on p.56-57 of *Bellan* [2006]). This means that one can draw an arbitrary closed contour  $C$  in three-dimensional space, define  $S$  as the surface for which this contour is a perimeter, and then the flux  $\int_C \mathbf{B} \cdot d\mathbf{s}$  will remain the same if the contour moves with the plasma. Since the contour is arbitrary this means that one could draw a first contour in one plane (e.g., the  $xy$  plane) and another contour in an orthogonal plane (e.g., the  $yz$  plane) and the two separate fluxes respectively linked by each of these initially orthogonal contours would remain constant as the contours deform because of plasma motion.

## 4. Discussion of the experiments and their main results

### 4.1. Flux rope self collimation and associated axial flows

Collimation, i.e., uniform cross-section along the length, is a striking feature of both actual solar corona loops and the scaled-down replicas produced in the Caltech laboratory experiments. This filamentary structure is counter to what was expected by solar observers (e.g., see *Klimchuk* [2000]) because it was presumed that the axial magnetic field of a loop would weaken with increasing distance from the solar surface. Since the flux  $BA$  is constant along a flux tube, weaker  $B$  should mean larger cross-sectional area  $A$ . The observed near-uniformity of  $A$  along the flux tube indicates that the axial field  $B$  is nearly constant along the length of the flux tube and is not getting weaker as was expected.

Collimation is observed in the single coronal loop (see Fig. 2(right)), in the spider legs (see Fig. 3), and in the jet plasma resulting from the merging of the spider legs in

Fig.3. These observations motivated a model to explain collimation [Bellan, 2003]. This model shows that when electric current is made to flow along an uncollimated magnetic flux tube, MHD forces drive axial plasma flows from the thin (small cross-section) to fat (large cross-section) parts of the flux tube. In the case of coronal loops this thin to fat motion corresponds to driving flows from both footpoints towards the apex. On the flux tube axis these forces are in the form of axial pressure gradients because there can be no magnetic force along the axis while off-axis the forces are the axial component of the  $\mathbf{J} \times \mathbf{B}$  force. Axial pressure gradients exist on the axis because the radial pinch force is stronger where the flux tube radius  $a$  is small than where  $a$  is large since for a given total axial current the pinch force scales as  $a^{-4}$  as discussed in Section 3.3. Radial pressure balance then results in a larger on-axis pressure where  $a$  is small (i.e., footpoints) than where  $a$  is large (i.e., apex). As sketched in Fig. 4 which is a straightened-out version of an arched flux tube, these axial flows carry frozen-in azimuthal magnetic flux from the footpoints to the apex (at  $z = 0$  in Fig.4) where the convected azimuthal magnetic flux and the flowing plasma accumulate. However, accumulation of azimuthal magnetic flux means that the azimuthal magnetic flux density is increasing and since magnetic field strength is the same as flux density, the azimuthal magnetic field  $B_\phi$  increases. The pinch force associated with the increased  $B_\phi$  squeezes down the radius of the fat midsection of the flux tube and so causes the flux tube to become collimated. Collimation is thus associated with flows from both footpoints filling the flux rope up with plasma [see Figs.1(b) and (c)]; this was called the “gobble” model because it appears as if the initial arched flux rope ingests plasma at its footpoints. The gobble effect can also be seen from examination of the induction equation [Bellan et al., 2005] which can be configured

for a straight axis flux rope to show that  $B_\phi/\rho r$  is invariant at the axial midpoint where the opposing flows collide ( $z = 0$  plane in Fig.4). This means that increasing  $\rho$  at  $z = 0$  and at some given radius  $r$  as a result of inflowing plasma necessarily increases  $B_\phi$  and so causes pinching; the radius  $a$  has to decrease to maintain  $2\pi a B_\phi = \mu_0 I$  where  $I$  is the axial current flowing from left to right in Fig.4. At the stagnation layer where the flows from the left and from the right collide ( $z = 0$  layer in Fig.4) there cannot be a directed flow and so the kinetic energy of flow must be converted into heat via collisions; this is somewhat of an oversimplification because the counterstreaming flows will in reality flow through each other for some distance and then dissipate because of collisions between the counterstreaming motions. Thus, the stagnation of the flows heats the plasma. The gobble model thus provides a self-consistent and testable hypothesis for why magnetic flux tubes having an axial electric current are bright, hot, plasma-filled, and collimated. Experiments testing the gobble model have supported this model. For example, the MHD  $\mathbf{J} \times \mathbf{B}$  axial forces predicted by the gobble model have been directly observed by *Haw and Bellan* [2017] using an array of magnetic probes that measured the time-dependent vector magnetic field over a large volume. The current density  $\mathbf{J}$  was determined using  $\mathbf{J} = \mu_0^{-1} \nabla \times \mathbf{B}$  and then the component of  $\mathbf{J} \times \mathbf{B}$  parallel to the flux rope axis was seen to be such as to drive flows from both ends (footpoints) of the flux rope towards the middle (apex). This measurement showing magnetic forces driving flows from both ends towards the middle is shown in Fig.5. Single-ended flows such as in Fig.3 are similarly collimated as discussed in *Bellan* [2018c, a, b]. MHD-driven flows have also been discussed by *Shibata and Uchida* [1986].

The gobble model prediction of upflows from both footpoints should be observable as Doppler blueshifts for an observer looking towards the footpoints. These blueshifts at both footpoints of the laboratory replica of a solar corona loop have been observed by *Tripathi et al.* [2007] and these observations are shown in Fig.6. Spectroscopic measurements of Doppler shifts of emission lines from hot ions in the upper transition region and corona at the center of the solar disk made by *Peter and Judge* [1999] using the SUMER instrument on the SOHO spacecraft have also indicated blueshifts with an average value corresponding to upflows of the order of 5 km/s. The solar blueshifts reported by *Peter and Judge* [1999] are thus consistent with the gobble model prediction of upflows from footpoints of solar corona loops and would be the result of averaging over a multitude of solar loops.

*Stenson and Bellan* [2008] vividly demonstrated the flows originating from the footpoints using a scheme where different gases were injected at the two footpoints. *Stenson and Bellan* [2008] generated Fig. 7 by putting atomic line filters in front of the camera to distinguish the two gases from each other. The composite red/purple color-coded image in Fig. 7 was then constructed from two camera images using a computer. Because the red gas (hydrogen) in Fig. 7 is lighter than the purple gas (nitrogen), the red gas goes faster and further and thus fills up a larger fraction of the flux tube. This figure also shows that the flux tube major radius increases as the lengths of the two jets increase. The flow velocity, being driven by magnetic forces, greatly exceeds thermal velocities [*Stenson and Bellan*, 2012; *Kumar and Bellan*, 2009]; this is consistent with having  $\beta \ll 1$ . Plasma density in the arched loop results from the plasma ingested by the jet upflow; this density is orders of magnitude larger than the density of the neutral gas initially puffed in to

enable breakdown [You *et al.*, 2005]. The magnetic configuration thus depends on the mass flux boundary condition as well as on the magnetic and electric current boundary conditions.

## 4.2. Eruptions

The gobble model addressed flows along the axis of a flux tube having a straight axis, an initially axially non-uniform cross-section, and an axial current. The gobble model showed that the axial flows would tend to fill the flux tube with plasma and collimate the flux tube. The gobble model did not take into account the curvature of the flux tube axis, i.e., the arch-shape of a solar loop. This curvature of the axis, introduces a more global effect wherein current flowing along a curved axis produces forces that tend to increase the radius of curvature. Since the effect of pressure gradients along the axis have already been taken into account in the gobble model, the analysis of the force resulting from the curvature of the current to lowest order involves magnetic forces only.

A solar loop can be considered a half toroid and so the axial current flowing from one footpoint to the other will produce hoop forces (magnetic pressure) that tend to increase the major radius of the half toroid. These currents have to be sufficiently strong to overcome the magnetic curvature force which is directed so as to oppose increase of the major radius. The competition between magnetic pressure and magnetic curvature forces is like having to blow hard enough to inflate a balloon where blowing corresponds to the hoop (magnetic pressure) force and the restraining force of the stretched balloon material corresponds to the magnetic curvature force.

The hoop force on a torus can be quantified by consideration of a virtual displacement of the major radius  $R$  of a flux-conserving toroid having minor radius  $a$  and toroidal current

I. A flux-conserving reduction of the system magnetic energy can be accomplished by the torus increasing its inductance since in electric circuit terms magnetic energy  $W$  can be expressed as  $W = LI^2/2 = \Phi^2/2L$  where  $L$  is the toroid inductance and  $\Phi = LI$  is the magnetic flux linked by the toroid. Since  $L$  is approximately proportional to the major radius, a flux-conserving increase of  $L$  reduces  $W$ . A more exact analysis based on the classic tokamak calculation by *Shafranov* [1966] is given in *Stenson and Bellan* [2012] where it is shown that the rate of change of the major radius  $R$  as a result of this force can be expressed as

$$\frac{d^2 R}{dt^2} = \frac{\alpha}{4\pi^2} \frac{\mu_0}{\rho a^2} \frac{I(t)^2}{R(t)} \quad (8)$$

where  $\alpha = \ln(R/a) + 1.08 + l_i/2$ ,  $l_i$  is the torus internal inductance, and  $\rho$  is the mass density. Equation (8) is a low  $\beta$  form of Eq.1a and has an exact analytic solution if the current can be approximated as rising linearly with time; i.e., if the current can be expressed as

$$I(t) = I_0 t / \tau. \quad (9)$$

This exact solution is obtained by substituting Eq. (9) into Eq. (8) to obtain

$$R(t) = \frac{1}{2\pi} \sqrt{\frac{\mu_0 \alpha}{2\rho}} \frac{I_0}{a\tau} t^2 \quad (10)$$

which is consistent with the experimentally observed dependence  $R \sim t^2$  when  $I \sim t$  as presented in *Stenson and Bellan* [2012].

### 4.3. Merging of coronal loops having same-sign or opposite-sign magnetic helicity

Magnetic helicity, is an important parameter characterizing magnetized plasmas because consideration of magnetic helicity provides insights regarding how a system tends to evolve. Magnetic helicity has a precise mathematical definition and can be interpreted

intuitively in various equivalent ways: for example, it can be thought of as a measure of the linkage of flux tubes with each other or as the twist of a flux rope. Magnetic helicity has many properties relevant to laboratory experiments and solar corona structures. Only a brief summary of the main features of magnetic helicity will be given here as magnetic helicity has been discussed extensively in the literature [*Woltjer, 1958; Calugareanu, 1959; Moffat, 1978; Berger and Field, 1984; Jensen and Chu, 1984; Finn and Antonsen, 1985; Pfister and Gekelman, 1991; Bellan, 2006, 2018c*].

The appropriate definition of magnetic helicity depends on whether the system under consideration is isolated or not. If the system is isolated, that is if no magnetic field lines exit the volume under consideration, then the magnetic helicity is simply  $K = \int \mathbf{A} \cdot \mathbf{B} d^3\mathbf{r}$  and because no field lines exit the volume this definition is gauge-independent. However, when field lines exit the volume under consideration, a considerably more complicated definition, called relative helicity must be used. The definition of relative helicity has the property of counting only those linkages existing within the volume under consideration while excluding all linkages that occur outside this volume. Because magnetic helicity characterizes general topological properties of a system rather than specific geometric details, it conceptually unifies a great range of phenomena that otherwise would seem unrelated. Injecting electric current to flow between two electrodes linked by an initially potential magnetic flux as in Fig. 1 corresponds to injecting helicity into a non-isolated system. Similarly, the situation shown in Fig.3 which has a considerably different geometry, also corresponds to injecting helicity into a non-isolated system.

Using the helicity concept identifies several important properties of a magnetized plasma (proofs given in the literature cited above):

1. Magnetic helicity has a sign such that a system with right-handed twist has positive helicity and a system with left-handed twist has negative helicity. Positive helicity corresponds to having an axial current that is parallel to the axial magnetic field; negative helicity has a current that is anti-parallel.

2. When magnetic reconnection occurs in an isolated system, magnetic helicity is nearly conserved whereas magnetic energy is dissipated. This means that after many reconnections the system evolves to a lowest energy state while retaining almost all its original helicity. This final minimum-energy, helicity-conserving state is called a Taylor state and the process of attaining this state is called Taylor relaxation. The Taylor relaxation analysis ignores dynamics because it assumes that the system slowly evolves through a sequence of equilibria with progressively lower magnetic energies until the minimum energy state is reached. The experiments described here were initially assumed to be describable by a Taylor relaxation process, but it was then discovered that there is no slow evolution through a sequence of equilibria because the system is highly dynamic. Also, the Taylor state ignores pressure gradients and focusses exclusively on the magnetic field whereas the systems discussed here are defined by the existence of bright regions (localized high pressure) that clearly show the magnetic field topology. Thus, the Taylor relaxation concept can be considered a useful starting point but not a complete description. The Taylor model describes the magnetic field and omits description of what the plasma is doing (e.g., has localized pressure, has flows, tends to self-collimate).

3. Mathematically, the Taylor state is a zero-pressure, force-free equilibrium governed by the relation  $\nabla \times \mathbf{B} = \lambda \mathbf{B}$  where the parameter  $\lambda$  can be interpreted in a number of equivalent ways: (i)  $\lambda$  is an eigenvalue, (ii)  $\lambda$  is the ratio of axial magnetic current

to axial magnetic flux, (iii)  $\lambda$  is the ratio of magnetic energy to magnetic helicity in an isolated system, (iv)  $\lambda$  is a measure of the twist, (v)  $\lambda$  is of the order of the inverse of the characteristic scale length of the system. Because helicity is conserved better than energy, combination of interpretations (iii) and (v) in this list shows that, if allowed, an isolated system will tend to expand in size because expansion provides a helicity-conserving decrease in stored magnetic energy.

4. When the system is not isolated as is the case in the experiments and in the solar corona, properties of magnetic helicity also depend on the time scale under consideration. On long time scales, substantial helicity might be injected into the system so the helicity is not conserved (e.g., the lengthening jet in Fig.3) but on very short time scales where negligible helicity is being injected, the system can be considered helicity-conserving (e.g., time scale of kink instability in Fig.3).

An experimental configuration having two adjacent solar corona loops was investigated by *Hansen et al.* [2004]. The configuration was such that the axial electric current was the same for the two loops but the directions of the respective axial magnetic fields could be the same or opposite. In the former case, the two loops have the same sign magnetic helicity while in the latter case, the two loops have opposite sign magnetic helicity. Two loops with the same sign corresponds to both loops having right-handed twist or both loops having left-handed twist; two loops with opposite sign helicity corresponds to one loop having right handed twist and the other left-handed twist.

Because of the attraction of the same-sense axial electric currents in the two loops, in both the same- and the opposite-helicity cases here the two loops attract each other and merge. However, the behavior of the merged loops is quite different. When loops having

the same sign of helicity merge (co-helicity merging), it is observed that the resulting single loop expands at a similar rate to that of a single loop but when loops with opposite-sign helicity merge (counter-helicity merging) the expansion is faster. Also, when counter-helicity loops merge there are substantial bursts of EUV radiation but not for co-helicity merging.

The interpretation for these differing behaviors is that loop expansion involves a competition between the magnetic pressure force ( $\nabla_{\perp} B^2$  force) which is directed to expand the loop major radius and the magnetic curvature force ( $\kappa B^2$ ) associated with stretching the axial magnetic field away from its initial vacuum-like configuration. Merging counter-helicity loops reduces the restraining magnetic curvature force while enhancing the expansive magnetic pressure force so as to cause faster expansion. Merging co-helicity loops retains both the restraining magnetic curvature force and the magnetic pressure force so the expansion rate stays about the same as for a single loop. Since the axial field is much larger than the azimuthal field in a weakly twisted loop, annihilation of the axial field as occurs in counter-helicity merging releases more magnetic energy than happens in co-helicity merging where it is the weaker, azimuthal field that is annihilated. This annihilation of a stronger magnetic field in the counter-helicity merging provides more energy for electron acceleration and explains why there are strong EUV bursts in the counter-helicity merging case but not in the co-helicity merging case.

Merging of coronal loops necessarily involves magnetic reconnection and dissipation. Dissipation is required because in order for reconnection to be a spontaneous process, it must involve a reduction of the potential energy stored in the configuration in analogy to a ball falling from the top of a hill to a valley being a spontaneous process but not

the reverse process. Since in a low  $\beta$  plasma the main form of stored energy is the magnetic field energy, reconnection must involve the system changing to a state of lower magnetic energy. This reduction in energy is accounted for by transformation of the removed magnetic energy into some combination of heat, energetic particles, or waves. Reconnection is required because the topology of the merged loops differs from that of the initial loops. Consider the merging of two identical simple flux loops each with axial flux  $\Phi_0$ , azimuthal flux  $\psi_0$ , axial length  $L$ , and axial cross-section  $A$ . According to the relation between linked flux and helicity each flux loop initially has a helicity  $K = 2\Phi_0\psi_0$  so the initial helicity of the two flux loops is  $K_{tot} = 2K = 4\Phi_0\psi_0$ . In order to keep  $K_{tot}$  constant, the merged structure will have axial flux  $\Phi_1 = \sqrt{2}\Phi_0$  and  $\psi_1 = \sqrt{2}\psi_0$ . There will have to be electric fields associated with this change in helicity-conserving change in flux and these electric fields will drive currents which produce the differential magnetic field that changes the topology, accelerate some particles to high energy, and act as the source for radiation of waves. These processes are not described by Eqs.1 but will be considered in Sec.4.9 where the effects of including resistive, Hall, and electron inertia terms in the generalized Ohm's law will be addressed.

#### 4.4. Strapping field and the torus instability

The hoop force can be opposed not only by the curvature force but also by imposition of an extra magnetic field produced by external coils. This additional magnetic field is arranged to be normal to the plane of the axis of the arched loop as sketched in Fig.8. If the loop is considered to be a half toroid and a cylindrical coordinate system  $\{R, \phi, z\}$  is used so that the current along the loop axis is in the  $\phi$  direction, then an external magnetic field in the  $z$  direction will produce a force  $J_\phi \hat{\phi} \times B_z \hat{z} = J_\phi B_z \hat{R}$ . This external

field  $B_z$ , called the strapping field, opposes the hoop force if the sign of the strapping field is such that  $J_\phi B_z$  is negative. An experiment with an externally produced strapping field by *Hansen and Bellan* [2001] showed that a sufficiently strong strapping field inhibits the eruption as predicted; this is shown in Fig. 9.

The torus instability was proposed by *Kliem and Torok* [2006] and involves a strapping field that decays with altitude at a specific rate (decay index). At low altitude the strapping field is sufficiently strong to oppose the hoop force but at high altitude the strapping field weakens and becomes incapable of opposing the hoop force. If the strapping field increases with altitude up to some critical altitude, but thereafter decreases with altitude, a loop at low altitude will be stable with respect to slight increases in axial current. This is because a slight increase in axial current will give a slight increase in hoop force which will push the arched loop up slightly higher until its apex reaches an altitude at which the strapping force becomes sufficiently strong to balance the hoop force. However, if the loop is above the critical altitude, a slight increase in current will again give a slight increase in hoop force but now there will be a loss of equilibrium because at higher altitude the strapping field is weaker and so cannot balance the increased hoop force. This loss of equilibrium results in an uninhibited upward expansion, i.e., an eruption. *Ha and Bellan* [2016] set up an experimental situation where a strapping field with a suitably short spatial decay length was produced by coils inside the vacuum chamber and observed that an erupting plasma loop accelerated when it penetrated this region of rapidly decaying strapping field. This experimentally observed initial inhibition of expansion followed by a fast expansion is shown by the IS data in Fig.10. This localized acceleration when the

loop apex attains the altitude where the strapping field decays is similar to that observed in numerical models, such as Fig.9 in *Fan* [2017].

#### 4.5. Apex Dips

A distinct dip at the apex of the laboratory experiment replicas of solar coronal loops is typically observed (see example in Fig.2(right)). For many years this dip was presumed to be the projection of a kink but recently *Wongwaitayakornkul et al.* [2017] determined that the dip occurs because there is higher mass density at the apex than elsewhere on the loop. The reason for this higher density is understood by consideration of the neutral gas jets sketched in green in Fig.1(a). Two possible situations can occur just before breakdown depending on the magnitude of the neutral gas collision mean free path compared to the characteristic dimension of the loop apex region. These are: (i) at the apex the injected neutral gas mean free path is very large so that the left and right neutral gas jets pass right through each other in which case the neutral gas density at the apex is just the linear sum of the right and left densities, and (ii) at the apex the neutral gas jets are so dense that the neutral gas collision mean free path is very small so the left and right jets collide resulting in a strong peaking of gas density at the apex in which case the apex gas density greatly exceeds the linear sum of the right and left densities. When ionization occurs in case (ii), the apex will have a much greater plasma mass density  $\rho$  than at loop locations away from the apex and so using Eq.8 it is seen that  $d^2R/dt^2$  will be smaller at the apex than at other locations because  $\rho$  is larger at the apex. This greatly reduced acceleration of the apex compared to elsewhere on the loop means that the apex will lag behind and this lag (reduced increase of major radius with time) appears as a dip at the apex.

This interpretation was confirmed by adjusting the amount of injected gas so as to be in case (i) or (ii). For low injected gas density there is minimal dip as shown in Fig. 11(left) while for high injected gas density there is a pronounced dip as shown in Fig. 11(right). Furthermore, by adjusting the relative timing of the left and right footpoint gas valves it was possible to move the region of high density to the left or right of center. As shown for the red and cyan cases in Fig. 12, the location of the dip moved off center and was located where the mass density was highest. Finally, an erupting loop with higher density at the apex was simulated using a 3D numerical MHD code. The numerical simulation shows an apex dip essentially identical to that observed experimentally as can be seen by comparing the experimental image in Fig.13(left) with the synthetic image created from the numerical simulation shown in Fig.13(right). This understanding of the apex dip has important implications for the solar context because it shows that the acceleration of each segment of a flux rope is inversely related to the mass density in the specific segment, i.e., it reveals the importance of mass loading, a dependence missing from both potential and force-free field models of the solar corona. This may be relevant to the static equilibrium of prominences where dips are observed to occur at regions of high localized density [Su and van Ballegooijen, 2012]. In the prominence situation, static upward  $\mathbf{J} \times \mathbf{B}$  forces compete with the downward solar gravity so in locations of greater local mass density, the gravitational force is locally greater resulting in a dip. The lab experiment has no gravity and instead dynamic  $\mathbf{J} \times \mathbf{B}$  forces accelerate the loop major radius and where the material being accelerated is locally more massive, there is less acceleration resulting in the heavy material lagging, producing a dip. From a mathematical point of view, the solar situation can be considered as characterized by the equation  $0 = \mathbf{J} \times \mathbf{B} - \rho\mathbf{g}$  while

the lab situation can be considered as characterized by  $\rho d\mathbf{U}/dt = \mathbf{J} \times \mathbf{B}$ . Thus, if the lab-relevant equation is written as  $0 = \mathbf{J} \times \mathbf{B} - \rho d\mathbf{U}/dt$  it is seen that the effective gravity is  $d\mathbf{U}/dt$  and that in both the lab and solar situations there will be a dip associated with regions of locally increased  $\rho$ .

#### 4.6. Coronal Mass Ejection Cavity

Coronal mass ejections are eruptive solar events having a characteristic three part structure consisting of a bright core surrounded by a dark cavity which in turn is surrounded by a bright leading edge; this structure is indicated in Fig.14(a). *Haw et al.* [2018] studied a solar coronal loop experiment where the vacuum chamber was prefilled with low density neutral gas of a different species from that used to make the loop. The experimental setup is sketched in Fig.15. Filters placed in front of the camera distinguished the laboratory replica of a coronal loop light from that of the background gas. Because the two gas species were different, the background gas plasma (hydrogen) could be represented as blue and the laboratory replica coronal loop (argon) could be represented as red in the computer-created composite images of the experimental measurements shown in Fig.14(b).

The outstanding feature of these measurements is the appearance of a dark gap between the red loop and the adjacent bright blue feature which is parallel to the red loop. The bright blue region was determined to be a reverse current region, i.e., a region where the electric current density  $J_y$  has the opposite sense of the current density in the laboratory replica coronal loop; the coordinate system in Fig.15 defines the  $y$  direction.  $J_y$  was determined by combining Ampere's law, the overall structural motion at a vertical velocity

$v_z$  and the much stronger dependence of  $B_x$  on  $z$  than  $B_z$  on  $x$  to give  $\mu_0 J_y = \partial B_x / \partial z - \partial B_z / \partial x \simeq \partial B_x / \partial z \simeq v_z^{-1} \partial B_x / \partial t$ .

The reversed current develops because the exterior region plasma (blue) is a magnetic flux conserver so a reversed current is required to shield the magnetic field produced by the red current. The reversed current is essentially like the eddy current induced on the surface of a copper sheet next to a pulsed wire. The eddy current creates a magnetic field equal and opposite to the field from the wire in order to have no net magnetic field in the copper sheet. Because anti-parallel currents mutually repel, the blue current is repelled by the red current leaving a void or cavity in between. Langmuir probe measurements of density show a density depletion in the region between the red and blue currents. A 3D numerical MHD model produces synthetic images as shown in Fig.14(c) similar to both those of the experiment and an actual CME. In addition to the experimental and numerical results *Haw et al.* [2018] also provide an analytic model for this repulsion associated with flux conservation in the external region.

The motion of the blue reversed current into the background plasma corresponds to the blue reversed current acting like a fast-moving piston that compresses the background plasma. *Wongwaitayakornkul et al.* [2019] have shown that this piston motion can drive a shock wave in the background plasma and have proposed this CME-driven shock as an explanation for the Extreme Ultra Violet waves [*Long et al.*, 2017] that are often seen in association with CME's.

#### 4.7. Loss of confinement of energetic particles from flux ropes

*Tripathi et al.* [2007] observed in certain situations that a diffuse plasma jet shot upwards from the apex of a laboratory experiment replica of a solar corona loop. This was

interpreted by *Tripathi et al.* [2007] to be a particle orbit phenomenon and so was called a 'kinetic jet'. The kinetic jet was shown to be closely related to a situation well known in the context of neutral beam injection into a tokamak. In the tokamak context, an injected neutral beam quickly becomes ionized and so turns into an ion beam. The injected neutral beam can be arranged to be either parallel or anti-parallel to the tokamak toroidal current (co- or counter-injected) and so the resulting ion beam is either parallel or anti-parallel to the toroidal electric current. Ion beams produced in a tokamak by counter-injected neutral beams are observed to have much worse confinement than those of co-injected neutral beams; this behavior is supported by numerical particle orbit calculations (e.g., see *Mikkelsen et al.* [1997]).

Although the beam confinement and toroidal current configuration are essentially identical in the laboratory replica of a solar corona loop and a tokamak the means for producing the toroidal current differ. In a tokamak, the toroidal current in the plasma is established when the primary current of a so-called Ohmic heating transformer changes and attempts to change the magnetic flux linked by the toroidal plasma; the plasma toroidal current can be considered to be the one-turn secondary of the Ohmic heating transformer and this plasma current is such that its associated magnetic flux is equal in magnitude and opposite in sign to the flux change introduced by the Ohmic heating transformer. By this means the net flux linked by the tokamak toroidal plasma remains constant corresponding to there being no net toroidal electric field in the plasma. The laboratory experiment replicating a solar loop differs from a tokamak by being a half rather than full torus and instead of having an Ohmic heating transformer drive the toroidal current, the solar loop experiment has electrodes at the footpoints drive the toroidal current. In this case

the toroidal current is directly imposed by the external power supply (capacitor bank) connected across the electrodes ; this power supply is represented by the red cylinder at the bottom in Figs.1(b-d). Although there is an electrostatic potential drop going from one electrode to the other, there is no axial electric field to the extent that ideal MHD is valid because the axial electric field is given by  $E_{axial} = -\partial V/\partial s - \partial A_{axial}/\partial t$  which is zero because  $\partial A_{axial}/\partial t = -\partial V/\partial s$  where  $A_{axial}$  is proportional to the magnetic flux associated with the axial current. The increase of  $A_{axial}$  with time corresponds to the flux tube twisting up as the axial current increases. Thus, while the electrostatic potential drop is real and measurable it does not produce an electric field in the plasma because the electric field contribution produced by the electrostatic potential gradient is exactly cancelled by the inductive component of the electric field. From the point of view of the external power supply, it is as if this power supply were switched to be across an inductor so that the power supply voltage would appear across the inductor and this voltage would correspond to  $d/dt(LI)$ . The wire in the inductor would be perfectly conducting so there would be no electric field in this wire as the inductive component of the electric field would exactly cancel the electrostatic component. The electric current corresponds to a difference between the electron and ion mean velocities and is independent of the mass-weighted mean of these velocities, i.e., independent of the center of mass motion of the plasma.

The kinetic jet shooting up from the apex of the laboratory simulation of a solar loop is explained starting with the concept that upwards MHD-driven jets originate from both footpoints as sketched in Fig.4 and in Fig.1(b); the Doppler blue shifts of these jets are shown in Fig.6. This means that one of the MHD-driven jets is parallel to the electric

current while the other is anti-parallel. The ions in these jets can be considered to be ion beams and so one ion beam is parallel to the loop axial electric current while the other is anti-parallel. For simplicity, the flux rope will now be assumed to have a straight axis as sketched in Fig.4. Thus, the magnetic field is of the form  $\mathbf{B} = B_z \hat{z} + B_\phi \hat{\phi}$ . Consider an ion that has an initial infinitesimal radial displacement from the  $z$  axis and an initial velocity  $\dot{\mathbf{r}} = v_0 \hat{z}$  with no initial  $r$  or  $\phi$  velocity components. The radial component of the Lorentz equation  $m\ddot{\mathbf{r}} = q\dot{\mathbf{r}} \times \mathbf{B}$  can then be written as

$$m(\ddot{r} - r\dot{\phi}^2) = q(r\dot{\phi}B_z - v_z B_\phi). \quad (11)$$

If both  $B_\phi = 0$  and  $\ddot{r} = 0$  are assumed, Eq.11 reduces to  $\dot{\phi} = -qB_z/m$ , i.e., to cyclotron motion. Now suppose that  $B_\phi \neq 0$  and again assume  $\ddot{r} = 0$  in which case Eq.11 can be expressed as

$$\dot{\phi}^2 + \Omega\dot{\phi} - v_z \frac{\Omega B_\phi}{B_z r} = 0 \quad (12)$$

where  $\Omega = qB_z/m$ . Equation 12 is a quadratic equation in  $\dot{\phi}$  with solutions

$$\dot{\phi} = \Omega \frac{-1 \pm \sqrt{1 + 4 \frac{B_\phi v_z}{B_z \Omega r}}}{2}. \quad (13)$$

If  $1 + 4B_\phi v_z / (B_z \Omega r) < 0$  then Eq.13 has no real solution which means it was incorrect to assume  $\ddot{r} = 0$ . This situation occurs if  $v_z$  has the opposite sign of  $B_\phi$  and has magnitude

$$|v_z| > \frac{1}{4} \left| \frac{qB_z^2}{mB_\phi} r \right|. \quad (14)$$

Examination of Eq.11 shows that large positive  $-v_z B_\phi$  causes  $\ddot{r}$  to become large and positive so the ion is ejected radially from the flux rope. Numerical calculations of ion trajectories in *Tripathi et al.* [2007] show indeed that if  $v_z$  has the opposite sign of  $B_\phi$  and also has sufficiently large magnitude to satisfy Eq.14, ions are radially ejected from

the flux rope. A Hamiltonian analysis involving effective potentials arrives at the same conclusion by showing that an effective potential valley becomes an effective potential hill resulting in loss of radial stability. Having the opposite sign of  $B_\phi$  corresponds to the ion moving counter to the axial current, i.e., like a just-ionized counter-injected tokamak neutral beam. The radial ejection can be interpreted equivalently as resulting from the property that opposite currents repel since if  $v_z$  has the opposite sign of  $B_\phi$ , the ions with this  $v_z$  can be considered as a sub-current opposite to the main current.

*Tripathi et al.* [2007] conducted a set of experiments having different gas puff pressures. The different pressures produced correspondingly different jet velocities from the foot-points with lower pressures resulting in faster jets since the jet velocity is inversely related to the jet mass for a given force. It was observed that the kinetic jet originating from the apex only occurred when the jet was sufficiently fast. The escape was from the apex because confinement is weakest at the apex. Numerically calculated ion orbits for positive and negative  $v_z$  show radial unstable motion for sufficiently large negative  $v_z$ . If a uniform current density is assumed then  $B_\phi = \mu_0 J_z r / 2$  so Eq.14 can be expressed as

$$|v_z| > \frac{1}{2} \left| \frac{qB_z^2}{m\mu_0 J_z} \right|. \quad (15)$$

The ratio of axial current  $I = J_z \pi r^2$  to axial flux  $\Phi = B_z \pi r^2$  in the flux rope can be expressed using

$$\lambda = \frac{\mu_0 I}{\Phi} = \frac{\mu_0 J_z}{B_z} \quad (16)$$

which is closely related to a force-free equilibrium  $\nabla \times \mathbf{B} = \lambda \mathbf{B}$ , the difference being that Eq.16 pertains only to the axial components of the magnetic field and current whereas

the force-free equilibrium involves all components. Equation 15 can then be expressed as

$$\left| \frac{\lambda v_z}{\Omega} \right| > \frac{1}{2} \quad (17)$$

which is analogous to a finite-Larmor radius condition since  $v_z/\Omega$  is analogous to a Larmor radius. Since the left hand side of this criterion scales as  $B_z^{-2}$ , Eq.17 could only be satisfied in solar contexts having very fast ions and extremely weak magnetic fields. This might happen when energetic ions move near a magnetic null.

#### 4.8. Kink instability driving secondary Rayleigh-Taylor instability

The coaxial jet experiment is similar to the laboratory replica of a solar corona loop but has a coaxial geometry as shown in Fig.3. The jet can be considered a lengthening flux rope with a magnetic field given by  $\mathbf{B} = B_z \hat{z} + B_\phi \hat{\phi}$ . The jet kinks when it attains a critical length satisfying the Kruskal-Shafranov kink instability criterion [Kruskal and Tuck, 1958; Shafranov, 1970]. This criterion is essentially  $\mathbf{k} \cdot \mathbf{B} = 0$  where a perturbation  $\exp(ik_z z + im\phi)$  is assumed and  $k_z \hat{z} + (m/a) \hat{\phi}$  where  $k_z = 2\pi/l$ ,  $l$  is the jet length, and  $a$  is the jet radius. For  $B_\phi/B_z$  positive it is necessary to have negative  $m$  and the Kruskal-Shafranov analysis shows that  $m = -1$  is the unstable mode. Thus, the kink instability criterion can be expressed as  $q = 2\pi a B_z / (l B_\phi)$  where

$$q = 1 \text{ for instability} \quad (18)$$

$$q > 1 \text{ for stability;} \quad (19)$$

$q$  is known as the ‘safety factor’ in tokamak terminology. The jet has increasing length so  $l$  starts out small in which case  $q$  initially exceeds unity and the jet is stable. When the jet attains the critical length at which  $q$  drops to unity, the kink instability begins as seen at 10  $\mu$ s in Fig.3 and as has been verified in detail by Hsu and Bellan [2003]. The kink

instability grows exponentially and causes the jet to develop an exponentially growing corkscrew shape. An observer attached to the jet plasma would thus be displaced with exponentially increasing distance from the jet axis and so have an exponentially increasing velocity. The observer would therefore be accelerating and since gravity is the same as acceleration, the observer would experience an effective gravity like a passenger in an accelerating automobile.

The effective gravity sets the stage for another type of MHD instability, the magnetic Rayleigh-Taylor instability [*Kruskal and Schwarzschild*, 1954; *Chandrasekhar*, 1961], which is an extension of the conventional fluid Rayleigh-Taylor instability (RTI). The RTI takes place at the interface separating a heavy fluid on top of a light fluid. Because of gravity, at the interface ripples develop that cause portions of the heavy and light fluids to interchange and so lower the overall gravitational potential energy. *Moser and Bellan* [2012] observed that the effective gravity produced by the kink lateral acceleration resulted in a spontaneous development of RTI ripples. They further saw that this caused a change of the jet magnetic field corresponding to phenomena beyond the scope of ideal MHD, namely a magnetic reconnection as well as an abruptly-starting emission of radio waves in the whistler regime. Because whistler waves are at frequencies above the lower hybrid frequency and below the electron cyclotron frequency, whistler waves are in a frequency regime much higher than the MHD frequency regime which consists of frequencies much below the ion cyclotron frequency. *Chai and Bellan* [2013] observed that there was an enhancement of EUV emission at the location of the RTI, a dimming of visible light emission, and further characterized the emission of whistler radiation. *Marshall et al.* [2018] observed X-ray bursts coincident with the RTI. Thus, there is a well-defined sequence of

jet formation, jet kinking, and then kink-instigated RTI; coincident with the RTI there is enhanced EUV emission, visible light dimming, whistler radiation, and an X-ray burst.

The RTI consists of the small ripples indicated by the white arrows in Fig.16(a). A critical feature of the instigation of RTI by kink lateral acceleration is an inherent asymmetry because of the directed nature of the effective gravity. This asymmetry means that ripples develop only on the trailing side of the laterally accelerating jet [bottom side of jet in Fig.16(a)] with the result that the cross-section  $A$  of the jet is periodically choked. This periodic choking has the consequence that the axial current density  $J$  must increase at the locations of decreased cross-section since  $J = I/A$  where  $I$  is the electric current flowing along the jet. According to ideal MHD, a plasma is a perfect conductor, i.e., according to ideal MHD a plasma can support infinite  $J$ . However, just like a real, finite-dimension water pipe cannot carry an infinite number of liters per second, the presumption that a real plasma can carry an infinite  $J$  must fail at some physical limit where some physical phenomenon develops and impedes the relative motion between electrons and ions that constitutes the current. This limit is quantified by a ceiling on the electron drift velocity which is the mean electron velocity observed in a frame where the mean ion velocity is zero. If the jet axis defines the  $z$  direction, the axial electric current density is  $J_z = ne(u_{iz} - u_{ez})$  and so the electron drift velocity is then  $v_d = J_z/(ne) = I/(neA)$ ; the reduction of the current cross section  $A$  will thus increase  $v_d$ . The theory underlying plasma electrical resistivity is based on the assumption that  $v_d$  is small compared to all characteristic plasma velocities, i.e.,  $v_d$  is assumed small compared to the ion acoustic velocity  $c_s = \sqrt{\kappa T_e/m_i}$ , the electron and ion thermal velocities,  $v_{T\sigma} = \sqrt{2\kappa T_\sigma/m_\sigma}$ , the phase velocities  $\omega/k_z$  of any plasma wave, and the speed of light. If  $v_d$  approaches any of

these characteristic velocities, phenomena occur that cause the plasma to cease acting as a perfect conductor. For example if  $v_d$  approaches the ion acoustic velocity, ion acoustic waves become destabilized whereas if  $v_d$  approaches the electron thermal velocity then the electrons run away [Dreicer, 1959]. A closely related issue concerns scale lengths. The ideal MHD Ohm's law  $\mathbf{E} + \mathbf{U} \times \mathbf{B} = 0$  gives Eq.1a and is based on the assumption that Hall and electron inertia terms can be dropped from the generalized Ohm's law. The argument for dropping these terms is based on the characteristic scale length being larger than the ion skin depth  $d_i = c/\omega_{pi}$ . The RTI is experimentally observed to squeeze the jet radius to be of the order of  $d_i$  which implies that Hall and electron inertia terms will abruptly become important. These terms are associated with fast collisionless reconnection and also with whistler waves (see Chapter 19 in *Bellan* [2018c]). This squeezing of the flux rope to the  $d_i$  scale by the kink-instigated RTI has recently been reproduced numerically by *Wongwaitayakornkul et al.* [2020] in a 3-D numerical solution of the MHD equations.

The experimental observations indicate that waves are destabilized when the RTI ripples choke the current channel cross-section. Preliminary measurements indicate that the waves are in the whistler regime. The jet behaves as if a large resistor were spliced into the axial current circuit at the location of the RTI ripples and this causes several associated phenomena. First, there is a pronounced dimming of visible light emission at the ripple location as seen in Fig.16(a). At the same time and location there is an increase in extreme ultra-violet (EUV) radiation as reported in *Chai and Bellan* [2013]. The visible light dimming indicates that density is depleted at the RTI location and the enhanced EUV emission indicates simultaneous electron acceleration to high energy followed by collisions

with ions to produce ions in highly excited states, the decay of which radiates the EUV emission. These two effects suggest that at the RTI location a large inductive voltage drop  $LdI/dt$  is established in a direction such as to sustain the current flow. This  $LdI/dt$  voltage drop is indicated in Fig.16(b). Since the jet originates from a negative electrode, conventional current flows towards the electrode, and so in accordance with Lenz's law the electric field providing the  $LdI/dt$  voltage drop points toward the electrode to oppose the change in current. Thus, in Fig.16 the jet flows to the left and the inductive electric field points to the right. However, ions and electrons constituting the jet both flow to the left, away from the electrode; this is consistent with a rightward electric current direction by having the leftward electron flow velocity exceed the ion leftward flow velocity. The rightward direction of the inductive field will accelerate ions to the right and electrons to the left. Thus, the inductive electric field reduces the ion leftward flow velocity leading to density depletion at the RTI location and increases the electron leftward flow velocity leading to generation of energetic electrons that can produce EUV emission in the region of density depletion. It should be noted that the electron motion is not governed by a complete equation of motion, i.e., by a description of how forces change the electron momentum. Instead, the electron mass is assumed to be infinitesimal and consistent with the characterization of the plasma by the MHD equations, the electron velocity adjusts in such a way as to produce the electric current required by the combination of boundary conditions (axial current) and Maxwell's equations (azimuthal current). This setting to zero of the electron inertia is consistent with treatments of ideal perfect conductors and fails to take into account physics taking place on the length scale of the electron skin

depth  $d_e = c/\omega_{pe}$  and on the time scale of the electron plasma and cyclotron frequencies  $\omega_{pe}, \omega_{ce}$ .

This model of a large inductive voltage drop leading to oppositely directed ion and electron accelerations is closely related to the double layer concept proposed by *Alfvén* [1986] to describe the explosive inductive mechanism described by *Alfvén and Carlqvist* [1967] and by *Jacobsen and Carlqvist* [1964]. The mechanism is explosive because all inductive energy of an initially zero resistance system is dissipated at the localized small segment of an inductive circuit where the electrical resistance becomes finite for some reason. This is seen from the circuit equation  $IR + LdI/dt = 0$  where  $R$  is the resistance of the localized region; multiplying by  $I$  and integrating gives  $\int I^2 R dt = -LI^2/2$ .

Using a plastic scintillator, *Marshall et al.* [2018] observed a  $\sim 1 \mu\text{s}$  burst of  $\sim 6 \text{ keV}$  X-rays coincident with the RTI. This short X-ray burst is interpreted as resulting from a small cohort of electrons being collisionlessly accelerated to the full  $LdI/dt$  voltage drop [*Marshall and Bellan, 2019*]. Although the mean free path of the thermal electrons is only a few microns for the 2 eV temperature and high density of the jet which has a length of 10's of cm, statistical analysis shows that a small cohort of electrons can nevertheless be collisionlessly accelerated to high energy. The statistical argument is based on the fact that when an electron travels a collision mean free path, it has a  $1 - e^{-1} = 0.63$  probability of being scattered and so lose its directed momentum. However, this means that the electron has an  $e^{-1} = 0.37$  chance of not being scattered. If one considers the 0.37 fraction of the electrons that are not scattered, because these electrons are accelerated by the electric field after one mean free path their kinetic energy will have increased. Since mean free path is quadratically proportional to electron kinetic energy, the mean free path

for these unscattered electrons becomes larger. When this group of electrons travel the next, longer mean free path, again a 0.37 fraction will not scatter and these will develop an even longer mean free path. This process repeats so that ultimately a fraction  $e^{-N}$  of the electrons will have collisionlessly traveled  $N$  successive increasingly long mean free paths. Eventually these electrons will undergo a large angle collision and because of the rapid deceleration will emit X-rays. Thus, there will be a brief transient burst of X-rays as observed.

#### 4.9. Whistler wave emission associated with kink-driven Rayleigh-Taylor instability

The choking of the current channel to the ion skin depth by the kink-driven Rayleigh-Taylor instability resulted in phenomena beyond the scope of ideal MHD, namely a burst of X-rays, evidence of waves in the whistler regime, and a change in the magnetic topology indicating magnetic reconnection. The generalized Ohm's law,

$$\mathbf{E} + \mathbf{U} \times \mathbf{B} - \underbrace{\frac{\mathbf{J}}{ne} \times \mathbf{B}}_{\text{Hall}} + \underbrace{\frac{1}{ne} \nabla P_e}_{\text{electron pressure}} + \underbrace{\frac{m_e}{e} \frac{d\mathbf{u}_e}{dt}}_{\text{electron inertia}} = \underbrace{\eta \mathbf{J}}_{\text{resistive}}, \quad (20)$$

is essentially a re-arrangement of the two-fluid electron equation of motion and contains the electric field  $\mathbf{E}$  as one of its terms. Here  $\mathbf{U}$  is the center of mass velocity of the plasma,  $\mathbf{u}_e = \mathbf{U} - \mathbf{J}/ne$  is the mean velocity of the electrons, and all quantities are measured in the lab frame. On taking the curl of the generalized Ohm's law and invoking Faraday's law  $\nabla \times \mathbf{E} = -\partial \mathbf{B}/\partial t$  a generalized form of the induction equation results (see Sec.19.2 of *Bellan* [2018c] for a more detailed discussion). As discussed in Sec.2 a reference Alfvén velocity  $v_{A0} = B_0 \sqrt{\mu_0 \rho_0}$  can be defined on choosing a reference magnetic field strength  $B_0$  and a reference mass density  $\rho_0$ . Then, also as discussed in Sec.2, by additionally

choosing a reference scale length  $l_0$ , a reference time  $\tau_{A0} = l_0/v_{A0}$  is established. On defining normalized quantities  $\bar{\mathbf{B}} = B/B_0$ ,  $\bar{t} = t/\tau_{A0}$ ,  $\bar{\mathbf{U}} = \mathbf{U}/v_{A0}$ , and  $\bar{\rho} = \rho/\rho_0$  the normalized induction equation becomes [Bellan, 2018c]

$$\begin{aligned} \frac{\partial \bar{\mathbf{B}}}{\partial \bar{t}} = & \bar{\nabla} \times (\bar{\mathbf{U}} \times \bar{\mathbf{B}}) + \underbrace{\frac{1}{S} \bar{\nabla}^2 \bar{\mathbf{B}}}_{\text{resistive}} - \underbrace{\frac{d_i}{l_0} \bar{\nabla} \times [(\bar{\nabla} \times \bar{\mathbf{B}}) \times \bar{\mathbf{B}}]}_{\text{Hall}} \\ & + \underbrace{\frac{d_i}{l_0} \bar{\nabla} \times \left( \frac{1}{\bar{\rho}} \bar{\nabla} \beta_e \right)}_{\text{electron pressure}} - \underbrace{\frac{d_e^2}{l_0^2} \bar{\nabla} \times \frac{\partial (\bar{\nabla} \times \bar{\mathbf{B}})}{\partial \bar{t}}}_{\text{electron inertia}} \end{aligned} \quad (21)$$

where

$$d_i = \frac{c}{\omega_{pi}}, \quad d_e = \frac{c}{\omega_{pe}} \quad (22)$$

are the ion and electron collisionless skin depths and

$$S = \frac{l_0 \mu_0 v_A}{\eta} \quad (23)$$

is the Lundquist number. Collisionless skin depths and Lundquist numbers for the Caltech experiment, the solar corona, and the solar chromosphere are listed in Table 2; these are calculated from the respective parameters listed in Table 1. The ideal MHD Ohm's law, Eq.1b, results when the terms labeled resistive, Hall, electron pressure, and electron inertia are all dropped. Resistive MHD results when the term involving  $S$  is retained while the Hall, electron pressure and electron inertia are dropped. The finite value of  $S$  in resistive MHD enables magnetic reconnection (change of magnetic topology) to occur but the time scales predicted by resistive MHD are generally much slower than what is observed [Bhattacharjee *et al.*, 2001]. As can be seen from the form of the resistive term in Eq.21, the resistive term (term involving  $S$ ) is diffusive in nature. When the scale length  $l_0$  shrinks to be of the order of the ion skin depth  $d_i$  so  $d_i/l_0$  becomes of order unity, the Hall term becomes important and changes the structure of the equation in a very significant manner

as it introduces a cross-coupling between different components of the magnetic field; this cross-coupling does not exist in ideal or resistive MHD. Unlike the resistive term (term involving  $S$ ), the Hall term is not diffusive but instead is the fundamental term enabling whistler waves; these waves result from the cross-coupling between different components of the magnetic field mentioned above. In fact, the basic dispersion relation for whistler waves can be derived by retaining only the left hand side of Eq.21 and the Hall term and then linearizing these equations about a uniform background magnetic field. In the reconnection situation, the background magnetic field is very non-uniform and represents a current sheet or in three dimensions a flux rope so the situation is more complicated than that of whistler waves. The current sheet model is 2.5D as it involves vectors that have components in three dimensions but two dimensions of the equilibrium are ignorable (e.g.,  $y$  and  $z$  directions) and all vector components of perturbations depend on only two components; e.g., all components of all perturbation vectors might depend on  $x$  and on  $y$  but not on  $z$ . Analysis of Eq.21 in the limit where the Hall term dominates the right hand side shows there is a fast non-diffusive reconnection which takes place on the whistler time scale and where there is some generation of whistler waves [Yoon and Bellan, 2017, 2019a] as whistler waves are the uniform-magnetic field normal mode. A peculiar and identifying feature of whistler waves is that as a consequence of the cross-coupling of magnetic field components whistler waves involve a circularly polarized magnetic field perturbation. Furthermore, and somewhat surprisingly this circular polarization holds even if the wave is propagating obliquely relative to the background magnetic field [Verkhoglyadova et al., 2010; Bellan, 2013]. This latter fact indicates that whistler waves should be identifiable

even in situations where the direction of the background magnetic field is not known and/or changing over space and time.

The earlier observation of oscillations in the whistler frequency regime (i.e.,  $\omega_{ci} \ll \omega \ll \omega_{ce}$ ), the multitude of new transient phenomena that appear when the scale length decreases to be of the order of  $d_i$ , and the circular polarization of whistler waves even when oblique suggested that the characteristic circular polarization of whistler waves should be observable when the  $d_i$  scale is attained no matter what the direction of the instantaneous average magnetic field might be. *Haw et al.* [2019] designed, constructed, and used a special radio frequency (rf) magnetic probe that consisted of four separate three-coil clusters arranged to measure the local vector magnetic field. The four clusters were arranged in a tetrahedron formation so as to provide enough information to calculate the curl of the wave magnetic field  $\tilde{\mathbf{B}}$  and hence provide a measurement of the wave current  $\tilde{\mathbf{J}}$ . The wave vector  $\mathbf{k}$  was then determined by inverting Ampere's law  $i\mathbf{k} \times \tilde{\mathbf{B}} = \mu_0\tilde{\mathbf{J}}$  using a method described in *Bellan* [2016b]. This was done for each frequency  $\omega$  in a Fourier transform of the signal and so  $\mathbf{k}(\omega)$  was measured experimentally. *Haw et al.* [2019] showed that the experimentally measured dispersion relation was in agreement with the theoretical whistler dispersion relation. *Haw et al.* [2019] also measured the wave  $\tilde{\mathbf{B}}(t)$  as a function of time and showed that  $\tilde{\mathbf{B}}(t)$  was circularly polarized. Figure 17 shows the physical location of the probe (called quad-probe in the figure), Fig. 18 (middle) shows the observed circular polarization of the rf magnetic field, and Fig.19 shows that the measured dispersion relation is in good agreement with the theoretical whistler dispersion (purple shaded region).

#### 4.10. Observation of the dependence of the Rayleigh-Taylor instability wavelength on magnetic field strength

The Rayleigh-Taylor instability results when there is an effective gravity  $g$  at the interface between a dense gas and a diffuse gas. In the presence of a uniform magnetic field  $\mathbf{B}$  tangential to this interface, the Rayleigh-Taylor growth rate is given by [*Kruskal and Schwarzschild*, 1954; *Goedbloed et al.*, 2019]

$$\gamma^2 = kg - 2 \frac{(\mathbf{k} \cdot \mathbf{B})^2}{\mu_0 \rho} \quad (24)$$

where  $\rho$  is the density of the dense gas and the density of the diffuse gas is assumed to be negligible. If the wavevector  $\mathbf{k}$  is nearly co-aligned with  $\mathbf{B}$  this becomes

$$\gamma^2 = kg - 2 \frac{k^2 B^2}{\mu_0 \rho} \quad (25)$$

which gives maximum  $\gamma^2$  when  $g = 4kB^2/\mu_0\rho$ . This relation implies that if  $\mathbf{k}$  and  $\mathbf{B}$  are along the flux rope axis, the instability wavelength for maximum growth is related to the magnetic field strength by

$$\lambda \rho g = 8\pi B^2 / \mu_0 \quad (26)$$

where  $\lambda = 2\pi/k$ . Equation 26 shows that when the axial magnetic field is so strong that  $\lambda$  exceeds the length of the flux rope, it is not possible to fit an entire instability wavelength into the flux rope and so the flux rope will not have a Rayleigh-Taylor instability. However, if the magnetic field is weak, then  $\lambda$  will be short compared to the flux rope length and so the instability can take place. By operating the bipolar experiment with a relatively small bias magnetic field (axial magnetic field), *Zhang et al.* [2020] observed Rayleigh-Taylor instabilities associated with the acceleration provided by the hoop force caused by the current flowing along the arched flux rope. A series of plasma shots was made with different values of bias magnetic field and it was observed that the wavelength  $\lambda$  of

the Rayleigh-Taylor ripples increased with the bias magnetic field strength in a manner consistent with Eq.26. Figure 20a shows Rayleigh-Taylor ripples for weak (upper row) and strong (lower row) bias magnetic field strengths; it is seen that the wavelength is longer for the strong bias magnetic field. Figure 20b shows the scaling of  $\lambda$  with the voltage on the capacitor used to drive the bias magnetic field and Fig.20c shows a plot of  $s = \lambda \rho g$  versus a parameter proportional to the square of the bias magnetic field (this parameter was mis-labeled as  $y$  in the figure).

#### 4.11. Direct access to the ion skin depth scale by the kink instability

Section 4.8 described a sequence where lateral acceleration of a flux rope by a kink instability produced a large effective gravity that created the heavy-fluid-on-top-of-light-fluid environment wherein a Rayleigh Taylor instability developed. The Rayleigh Taylor ripples choked the jet cross-section down to the ion skin depth  $d_i = c/\omega_{pi}$  which corresponded to the electron drift velocity becoming so large that the assumptions of ideal MHD no longer hold. In particular, the plasma no longer behaved as a perfect conductor and instead behaved as if it had a large resistance. This interrupted the current flowing along the flux rope axis resulting in a large inductive voltage drop, generation of an X-ray burst, and emission of a burst of whistler waves.

By operating the experiment in a somewhat different regime, choking of the flux rope cross section down to  $d_i$  was observed by *Seo et al.* [2020] without the intermediate process of the kink driving a Rayleigh-Taylor instability. Here instead, the kink instability directly caused the flux rope cross section to be reduced to be of the order of  $d_i$ . The kink instability is an ideal MHD instability which means that the kink cross-section is presumed to be larger than  $d_i$  since, as comparison between Eqs.1b and 21 shows, ideal MHD is based

on the assumption that Hall terms can be dropped from the generalized Ohm's law and the condition for dropping these terms is that the scale length  $l_0$  exceeds  $d_i$ . However, one of the important properties of the kink instability is that it is an incompressible instability [Newcomb, 1960]. The kink process involves the initially straight axis of the flux rope becoming an exponentially growing helix. This process means that the flux rope axis length will increase. However, because kink incompressibility means that the flux rope volume remains constant during the instability, increase of the length of the flux rope axis means that the flux rope cross-section must decrease to maintain constant volume. This decrease of flux rope cross-section means that the scale length of the cross section can decrease to be less than  $d_i$  at which point the Hall term becomes important and ideal MHD no longer holds. Seo et al. [2020] observed this process in the coaxial configuration and saw that the aspect ratio (i.e., length/radius) of a flux rope increased as the flux rope underwent kink instability and that when the radius decreased to be of the order  $d_i$ , an X-ray burst, a whistler wave burst, and a change of magnetic topology (magnetic reconnection) occurred simultaneously. The X-ray burst is indicative of the sudden development of a large inductive electric field and is consistent with localized interruption of current because of localized increase in resistivity. The whistler wave burst is indicative that Hall terms are suddenly important as whistler waves are the characteristic mode associated with Hall term dynamics. The sudden change in magnetic topology is indicative of fast magnetic reconnection resulting from Hall and electron inertia terms that are neglected in ideal MHD.

#### 4.12. Transport Considerations

While the experiments have been largely directed towards investigation of ideal MHD physics, many phenomena beyond ideal MHD have been addressed to various extents such as accessing the Hall regime, excitation of whistlers, and X-ray production that have already been discussed. In addition, several issues relating to transport have been considered. While transport is often considered as an afterthought, it ultimately constrains important plasma parameters such as temperature and lifetime. Transport issues can be subtle since collisions between like-sign particles have drastically different consequences from collisions between opposite sign particles (see Section 5.6 in *Chen* [1984] and Section 2 in *O'Neil* [1995]). Specifically, ion-ion collisions provide viscosity but have no effect on electrical resistivity and hence no effect on the extent to which magnetic flux is frozen into the plasma. Similarly, ion-ion collisions have no effect on confinement of the bulk ions in a magnetic field. In particular, the ion-ion collision frequency can greatly exceed the ion cyclotron frequency so that even though no single ion ever completes an ion cyclotron orbit, magnetic flux remains frozen in to the collection of ions and the ions remain confined. Diffusion of the plasma center of mass (which is essentially the ion center of mass because  $m_i/m_e \gg 1$ ) results only from electron-ion collisions in the context of resistive MHD (see Section 5.5 of *Chen* [1984]).

Hydrodynamic concepts such as turbulence associated with a large Reynolds number are not applicable to a low  $\beta$  plasma such as the lab and solar plasmas discussed here. This is because consideration of Reynolds number relates to the competition between the non-diagonal components of the pressure tensor (these components scale as viscosity times velocity shear) and the convective component  $\rho \mathbf{U} \cdot \nabla \mathbf{U}$  of the fluid acceleration in

the Navier-Stokes equation. However, in MHD the Navier-Stokes equation is replaced by Eq.1a and in low  $\beta$  plasmas such as being considered here the magnetic force term greatly exceeds the divergence of the pressure tensor. The off-diagonal components of the pressure tensor are consequently second-order small since they are small compared to the gradient of the isotropic pressure which itself is small compared to the magnetic force. Since viscosity is essentially a description of how velocity shears create the off-diagonal components of the pressure tensor, viscous forces are relatively unimportant compared to other forces. Thus, while a Reynolds number (comparison of viscous term to convective term) can be calculated, it does not denote any specific regime such as turbulent or non-turbulent in a low  $\beta$  MHD plasma. Essentially, the plasma is well-frozen to the magnetic field and so if the plasma attempted to develop a hydrodynamic-type turbulence it would have to distort the magnetic field which would require more energy than is available in the pressure-gradient-driven turbulence. Instead, the plasma stability is characterized by MHD instabilities such as the kink and Rayleigh-Taylor instabilities which feed off the magnetic energy.

However, it is conceivable that while viscosity is small, it might contribute to heating the plasma by converting velocity shear into heat. The standard plasma transport equations are given by *Braginskii* [1965]. The basic viscosity is  $\eta_0 = 0.96n\kappa T_i\tau_{ii}$  (the use of eta to define viscosity leads to a possible confusion with resistivity which is also defined by eta in standard notation, but rather than change to a different symbol here for either viscosity or resistivity, the use of a subscript will mean viscosity and if there is no subscript then the meaning will be resistivity). Braginskii shows that when  $\omega_{ci}\tau_{ii} \gg 1$ , the viscosity depends on  $\eta_0, \eta_1, \eta_2, \eta_3$ , and  $\eta_4$  where  $\eta_1, \eta_2 \sim \eta_0/(\omega_{ci}\tau_{ii})^2$  and  $\eta_3, \eta_4 \sim \eta_0/(\omega_{ci}\tau_{ii})$ . The

Caltech lab experiment with parameters given in Table 1 has  $\omega_{ci}\tau_{ii} \ll 1$  so that in this experiment the viscosity only involves  $\eta_0$  which is listed in Table 2.

Using Eqs.(2.3i), (2.20), and (2.22) in *Braginskii* [1965] it is seen that the rate of ion temperature increase as a result of viscous heating is given by

$$\frac{3}{2}n \frac{d}{dt}(\kappa T_i) = \pi_{i\alpha\beta} \frac{\partial u_{i\alpha}}{\partial x_\beta} \quad (27)$$

where if  $\omega_{ci}\tau_{ii} \ll 1$

$$\pi_{i\alpha\beta} = -\eta_0 W_{\alpha\beta}. \quad (28)$$

If  $\omega_{ci}\tau_{ii} \gg 1$  then  $\pi_{i\alpha\beta}$  is given in *Braginskii* [1965] by a complicated expression involving  $\eta_0, \eta_1, \eta_2, \eta_3,$  and  $\eta_4$  so since  $\eta_0$  is larger by at least a factor of  $\omega_{ci}\tau_{ii}$  relative to the other components, Eq.28 can be considered an upper bound on the stress tensor. The quantity  $W_{\alpha\beta}$  in Eq.28 is a linear function of  $\partial u_{i\alpha}/\partial x_\beta$  and so for purposes of estimation we may assume that  $W_{\alpha\beta} \approx \partial u_{i\alpha}/\partial x_\beta$ . Equation 27 can then be expressed in the form of a bound on the viscous heating as

$$n \left( \frac{d}{dt}(\kappa T_i) \right)_{viscous} < \eta_0 \max \left| \frac{\partial u_{i\alpha}}{\partial x_\beta} \right|^2 \quad (29)$$

or using  $\eta_0 \approx n\kappa T_i \tau_{ii}$

$$\frac{1}{T_i} \left( \frac{dT_i}{dt} \right)_{viscous} < \tau_{ii} \max \left| \frac{\partial u_{i\alpha}}{\partial x_\beta} \right|^2. \quad (30)$$

The maximum velocity shear in the experiment is given by the Alfvén velocity divided by the radius of the current channel so using a current channel radius of  $0.01l_0$  and the ion-ion collision time  $\tau_{ii} \simeq 10^{-9}$  s given in Table 2, Eq.30 gives  $\left[ \frac{1}{T_i} \left( \frac{dT_i}{dt} \right)_{viscous} \right]^{-1} > 25 \mu\text{s}$  which is longer than the experimental time scale. This analysis thus shows that ion viscous heating will not be important. Furthermore, the assumed  $0.01l_0$  radius implies a 3 mm current channel radius for the lab experiment which is an overly conservative assumption

as this radius is less than the ion skin depth; at this scale ideal MHD is no longer valid and the whistler-related phenomena discussed in Section 4.9 would take place. However, this  $0.01l_0$  is being assumed here for consistency with comparison with the solar plasmas where a 100:1 aspect ratio is realistic and also to provide an easily calculable bound for viscous heating. In contrast to the viscous heating time, the electron-ion energy equipartition time for the lab experiment is  $0.25\mu\text{s}$  which is much shorter than the experimental time. Thus, the electrons heat up from resistive dissipation and then quickly share their thermal energy with ions via electron-ion collisions. Measurements by *Perkins* [2011] indicated that the Ohmic heating of the electrons (shared via collisions with the ions) in the Caltech lab experiment is balanced by EUV radiation to clamp the temperature to about 2 eV. The measurements by *Perkins* [2011] also show that the Ohmic heating power is only about 10% of the total input power with the remainder of the input power going into the translational kinetic energy of the expanding loop as well as the increase of magnetic energy in the loop as a consequence of its volume expanding while its internal magnetic field remains approximately constant.

Calculation of ion viscous heating for a solar corona loop having current channel radius of  $0.01l_0$  shows that the ion viscous heating time is 1 s which is approximately the same as the electron-ion energy equipartition time; however, the estimate for the right hand side of Eq.29 is probably excessive since actual velocities will generally be less than  $v_A$ , the more complicated expressions involving  $\eta_1 - \eta_4$  should be used, and  $\eta_1 - \eta_4 \ll \eta_0$ . The possibility that ion viscous heating can in certain circumstances play a role comparable to resistive heating in coronal loop plasmas has been shown by *Ofman et al.* [1994] and by *Erdelyi and Goossens* [1995].

Calculation for the solar chromosphere assuming again a current channel radius of  $0.01l_0$  shows that the ion viscous heating time is of the order of 700 s which greatly exceeds the electron-ion equipartition time of  $10^{-4}$  s. Thus, just as in the lab experiment, ion viscous heating is likely to be dominated by ion heating via electron-ion energy equipartition in both solar corona loops and in the chromosphere.

The Reynolds numbers for the lab experiment, solar corona loop, and chromosphere are listed in Table 2, but as mentioned earlier these have no real meaning in the context of low  $\beta$  MHD because low  $\beta$  means that MHD forces generally dominate pressure gradient terms including the off-diagonal terms associated with viscosity.

#### 4.13. Experimental results motivating new theoretical models

The experimental results discussed here revealed new behaviors that had not been predicted in any theoretical model and so in order to explain the observations new models were developed. In addition, simply working in the general topical area often motivated development of new models even without a specific experimental result. These models are not only relevant to solar physics, but also to magnetospheric physics and to astrophysics which can have similar physics but at very different scales from the lab or the sun. Examples of such theoretical models are:

1. A model showing why flux ropes tend to be collimated [*Bellan*, 2003]
2. A model for how accretion disks and astrophysical jets form a complete electric circuit that transfers angular momentum in a conservative way much like a generator transfers angular momentum via wires to a distant motor [*Bellan*, 2016a, 2018d]
3. A model providing a time-dependent analytic solution for an astrophysical jet [*Bellan*, 2020]

4. A model for how energetic particles are created in the presence of sub-Dreicer electric fields [*Marshall and Bellan, 2019*]

5. A model providing an intuitive explanation for fast collisionless magnetic reconnection [*Yoon and Bellan, 2017, 2019a*] in the electron MHD context, i.e., the context where the time scale is so fast that ions can be considered stationary, and the reconnection length scale is short compared to the ion skin depth so Hall terms and electron inertia are important.

6. A model showing that ions experience fast stochastic heating during fast collisionless reconnection [*Yoon and Bellan, 2018, 2019b*]

7. A model showing how the reverse current associated with coronal mass ejection drives extreme ultraviolet fronts in the solar corona [*Wongwaitayakornkul et al., 2019*]

## 5. Summary and Discussion

Laboratory experiments exhibit a wide range of phenomena that are scalable to the solar corona. Because the experiments are real, they automatically incorporate a completely self-consistent set of physics and so, in contrast to analytic or numerical models, do not contain any simplifying assumptions. By using increasingly sophisticated diagnostics and by careful arrangement of initial and boundary conditions, detailed information on a variety of physical phenomena can be obtained. Because the experiments are reproducible and have many controllable parameters, physical models can be quantitatively tested. The discovery of new and unexpected phenomena, such as kink instigation of Rayleigh-Taylor instability, stimulates development of new models relevant to the solar situation. Experimentally observed phenomena that are not directly scalable to the solar corona

are also useful because these raise questions of how such phenomena might occur in the solar context. Although the experiments scale well to solar situations to the extent that both can be described by ideal MHD, non-ideal phenomena typically cannot be directly scaled and may be different. An important difference of this sort involves the separation of scales having different types of physics, for example the separation between ideal MHD and Hall MHD. In the solar corona this separation of scales is extreme so that it is difficult to observe the Hall scale which is of the order of meters which is essentially infinitesimal compared to the ideal MHD scale which is millions of meters. The separation of scales between ideal and Hall MHD is much less in the experiment so it is possible to observe coupling between these scales. Addressing this difference leads to the concept that the solar corona does not have a single ideal MHD scale but rather has a range of ideal MHD scales arranged in a fractal fashion where the very smallest ideal MHD scale couples to the Hall scale. This concept is consistent with the fractal nature of observed solar phenomenon and in particular the property that when resolution is increased the phenomenology remains similar to what was seen at larger scales. A similar issue affects the Lundquist number which just barely satisfies the requirement of being large compared to unity in the experiment but is enormously larger than unity in the solar corona. This means that resistive phenomena cannot be directly scaled from the experiment to the solar corona, but it also means that any effect of finite resistivity is more easily seen. The electron drift velocity relative to ions is a much higher fraction of the Alfvén velocity in the lab experiment than on the sun and this means that the threshold for kinetic instability is lower in the experiment. While this again means that the experiment cannot be kinetically scaled to the solar corona, it also means that it is easier to resolve kinetic

phenomena in the experiment and so develop an understanding for underlying physics. The laboratory experiments thus provide an important and complementary contribution to the understanding of solar corona physics.

### *Acknowledgements*

This two decades of experimental research has been supported by grants from the NSF, USDOE, and AFOSR. The most recent are from the NSF/DOE Partnership in Plasma Science and Engineering via USDOE Grant DE-FG02-04ER54755, the Air Force Office of Scientific Research via Award Number FA9550-11-1-0184, the NSF SHINE program via Award 1059519, and the NSF Solar Terrestrial Research Program via Award Number 1914599.

All data are properly cited and can be accessed in the following references:

*You et al.* [2005], *Haw and Bellan* [2017], *Stenson and Bellan* [2008], *Hansen and Bellan* [2001], *Ha and Bellan* [2016], *Wongwaitayakornkul et al.* [2017], *Haw et al.* [2018], *Marshall et al.* [2018], *Haw et al.* [2019], *Zhang et al.* [2020], *Seo et al.* [2020]

### **References**

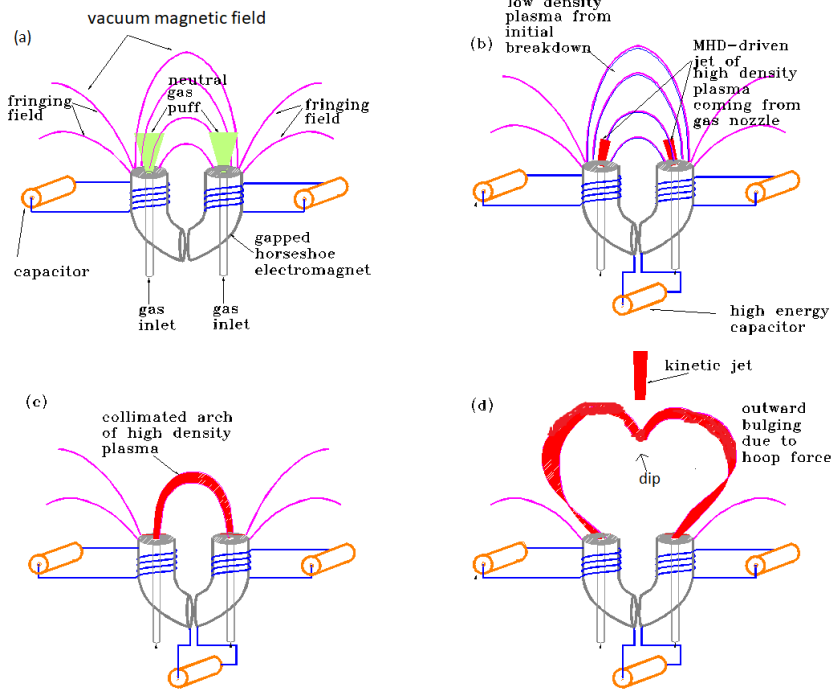
- Alfvén, H. (1986), Double-Layers and Circuits in Astrophysics, *IEEE Transactions on Plasma Science*, *14*(6), 779–793, doi:10.1109/TPS.1986.4316626.
- Alfvén, H., and P. Carlqvist (1967), Currents in the solar atmosphere and a theory of solar flares, *Solar Physics*, *1*(2), 220–228, doi:10.1007/BF00150857.
- Bellan, P. M. (2003), Why current-carrying magnetic flux tubes gobble up plasma and become thin as a result, *Physics of Plasmas*, *10*(5), 1999–2008, doi:10.1063/1.1558275.

- Bellan, P. M. (2006), *Fundamentals of Plasma Physics*, Cambridge University Press, Cambridge.
- Bellan, P. M. (2013), Circular polarization of obliquely propagating whistler wave magnetic field, *Physics of Plasmas*, *20*(8), 082,113, doi:10.1063/1.4817964.
- Bellan, P. M. (2016a), Integrated accretion disc angular momentum removal and astrophysical jet acceleration mechanism, *Monthly Notices of the Royal Astronomical Society*, *458*(4), 4400–4421, doi:10.1093/mnras/stw562.
- Bellan, P. M. (2016b), Revised single-spacecraft method for determining wave vector  $\mathbf{k}$  and resolving space-time ambiguity, *Journal of Geophysical Research: Space Physics*, *121*(9), 8589–8599, doi:10.1002/2016JA022827.
- Bellan, P. M. (2018a), Experiments and models of MHD jets and their relevance to astrophysics and solar physics, *Physics of Plasmas*, *25*(5), 055,601, doi:10.1063/1.5009571.
- Bellan, P. M. (2018b), Experiments relevant to astrophysical jets, *Journal of Plasma Physics*, *84*(5), doi:10.1017/S002237781800079X.
- Bellan, P. M. (2018c), *Magnetic Helicity, Spheromaks, Solar Corona Loops, and Astrophysical Jets*, World Scientific (Singapore ; Hackensack, NJ), doi:10.1142/q0151.
- Bellan, P. M. (2018d), Model for how an accretion disk drives astrophysical jets and sheds angular momentum, *Plasma Physics and Controlled Fusion*, *60*(1), 014,006, doi:10.1088/1361-6587/aa85f9.
- Bellan, P. M. (2020), Analytic Model for the Time-dependent Electromagnetic Field of an Astrophysical Jet, *The Astrophysical Journal*, *888*(2), 69, doi:10.3847/1538-4357/ab5f0d.

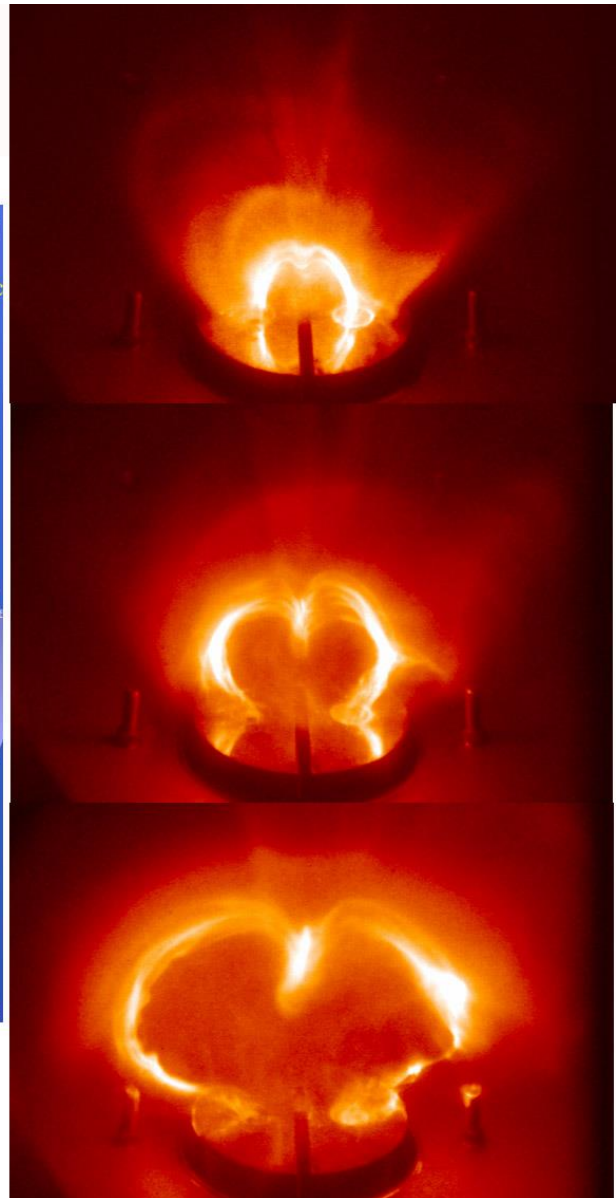
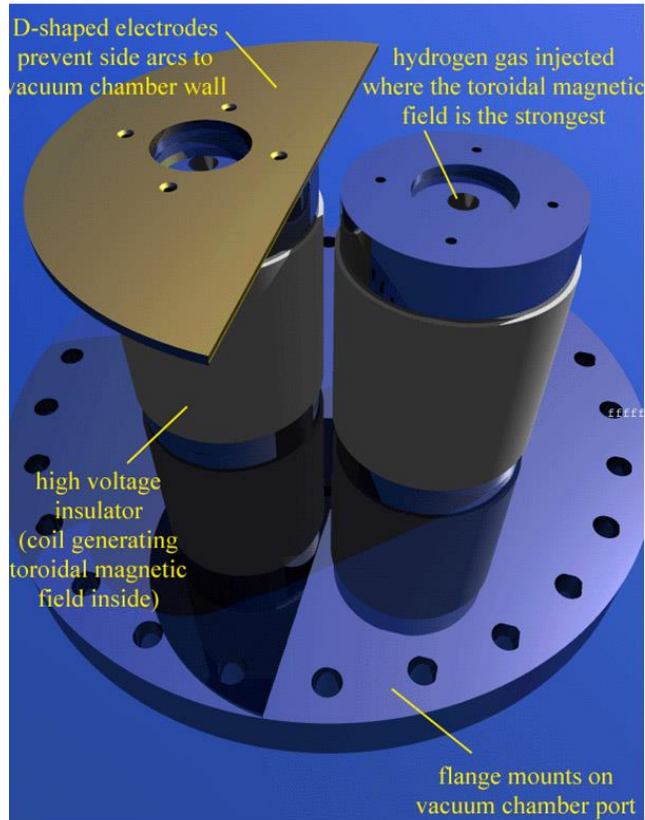
- Bellan, P. M., S. You, and S. C. Hsu (2005), Simulating Astrophysical Jets in Laboratory Experiments, in *High Energy Density Laboratory Astrophysics*, edited by G. Kyrala, pp. 203–209, Springer-Verlag, Berlin/Heidelberg.
- Berger, M. A., and G. B. Field (1984), THE TOPOLOGICAL PROPERTIES OF MAGNETIC HELICITY, *Journal of Fluid Mechanics*, 147, 133–148.
- Bhattacharjee, A., Z. W. Ma, and X. Wang (2001), Recent developments in collisionless reconnection theory: Applications to laboratory and space plasmas, *Physics of Plasmas*, 8(5), 1829–1839, doi:10.1063/1.1353803.
- Braginskii, S. I. (1965), Transport Processes in a Plasma, in *Reviews of Plasma Physics*, vol. 1, pp. 205–311, Consultants Bureau, New York, edited by M. A. Leontovich.
- Calugareanu, G. (1959), L'integrale de Gauss et l'Analyse des noeuds tridimensionnels, *Rev. Math. Pures Appl.*, 4, 5.
- Chai, K. B., and P. M. Bellan (2013), Extreme ultra-violet movie camera for imaging microsecond time scale magnetic reconnection, *Review of Scientific Instruments*, 84(12), 123,504.
- Chandrasekhar, S. (1961), *Hydrodynamic and hydromagnetic stability*, The International series of monographs on physics, Clarendon Press, Oxford, p.464.
- Chen, F. F. (1984), *Introduction to Plasma Physics and Controlled Fusion*, Springer US, Boston, MA, doi:10.1007/978-1-4757-5595-4.
- Chen, J. (2003), Acceleration of coronal mass ejections, *Journal of Geophysical Research*, 108(A11), doi:10.1029/2003JA009849.
- Chen, J., C. Marque, A. Vourlidas, J. Krall, and P. W. Schuck (2006), The Flux Rope Scaling of the Acceleration of Coronal Mass Ejections and Eruptive Prominences, *The*

Parameter	Symbol, units	Caltech Lab	Corona	Chromosphere
ion skin depth	$d_i$ , m	$8 \times 10^{-3}$	2	0.2
electron skin depth	$d_e$ , m	$3 \times 10^{-5}$	$5 \times 10^{-2}$	$5 \times 10^{-3}$
resistivity	$\eta$ , Ohm-m	$1.7 \times 10^{-4}$	$2 \times 10^{-6}$	$3.6 \times 10^{-4}$
Lundquist number	$S = l_0 \mu_0 v_A / \eta$	43	$8 \times 10^{12}$	$2 \times 10^8$
ion-ion collision time	$\tau_{ii}$ , s	$10^{-9}$	0.03	$2 \times 10^{-6}$
electron collision time	$\tau_e$ , s	$5 \times 10^{-12}$	$10^{-3}$	$5 \times 10^{-8}$
e-i energy equipartition time	$\tau_{E,ei}$ , s	$3 \times 10^{-7}$	2	$10^{-4}$
viscosity (Braginskii )	$\eta_0$ , kg m <sup>-1</sup> s <sup>-1</sup>	$10^{-5}$	$10^{-2}$	$10^{-6}$
ion magnetization	$\omega_{ci} \tau_{ii}$	$2 \times 10^{-3}$	$10^4$	1
Reynolds number	$l_0 v_A \rho_0 / \eta_0$	$10^6$	$5 \times 10^4$	$2 \times 10^8$

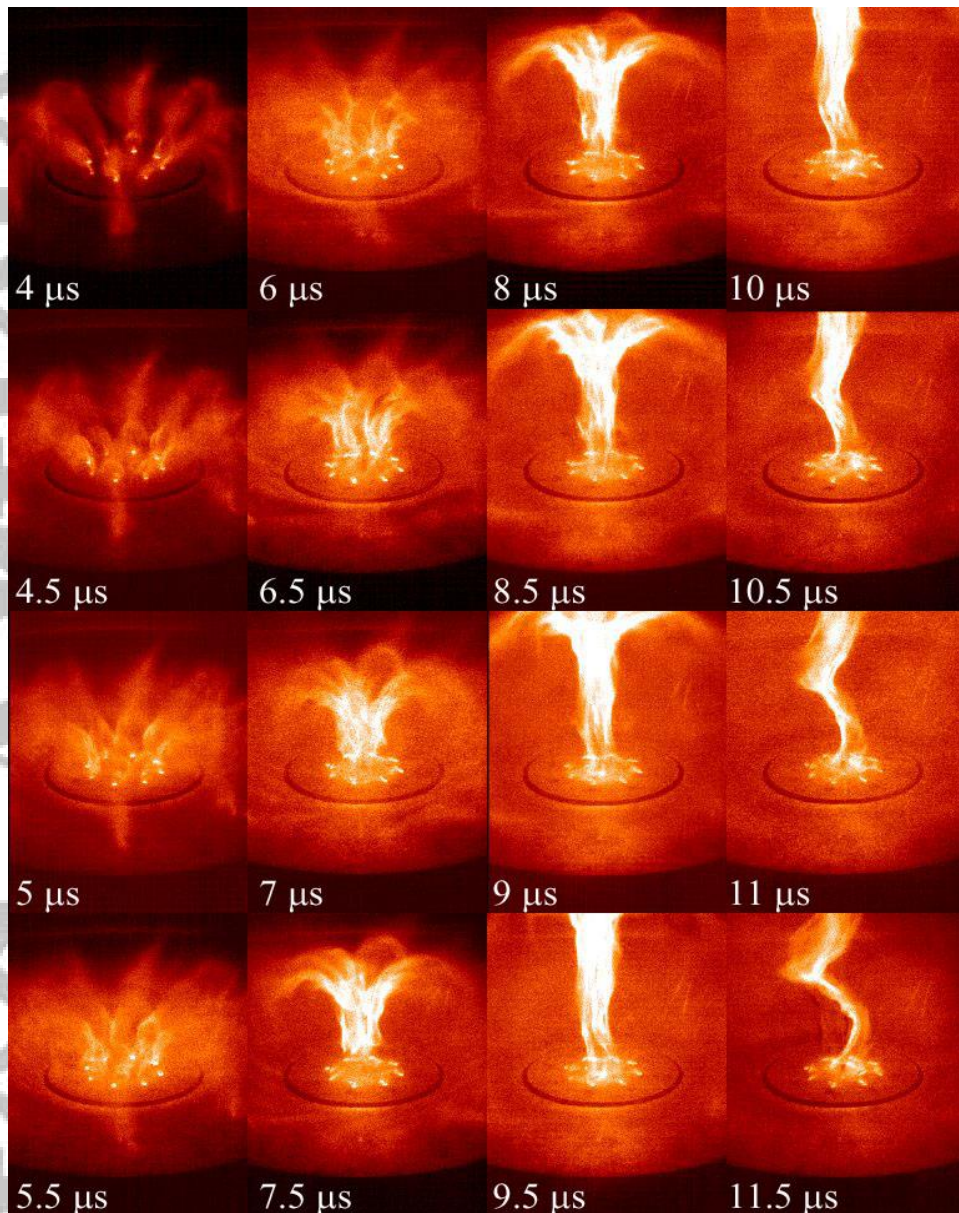
**Table 2.** Parameters that characterize properties beyond ideal MHD; these are all calculated from the reference parameters given in Table 1.



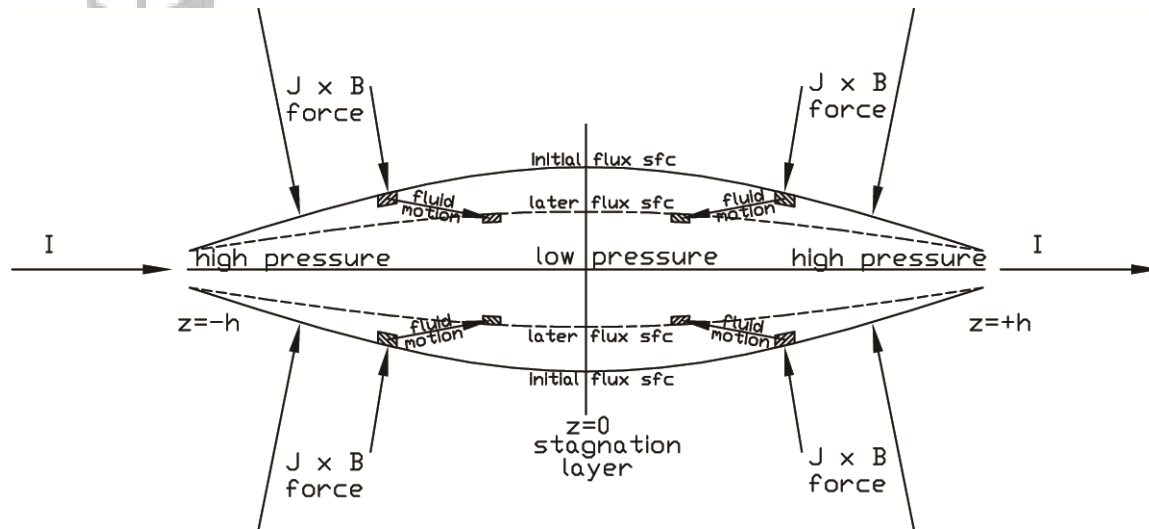
**Figure 1.** Bipolar source sequence of operation: (a) electromagnets are energized and neutral gas is puffed in; (b) high voltage is applied across electrodes breaking down neutral gas to form weakly ionized plasma, with increasing axial current MHD forces drive upward plasma jets from both footpoints; (c) the plasma flowing up from the footpoints forms a dense collimated loop; (d) the loop major radius expands from hoop force with optional dip at apex and optional kinetic jet.



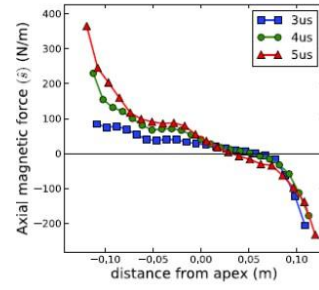
**Figure 2.** Bipolar configuration. Left: electrodes (D-shaped electrode used on both sides, but only left side shown here). Right: time sequence (increasing time going downwards) showing hoop force expanding major radius, collimation, and dip at apex. [Credit for figure on left: Hansen, J. F., and P. M. Bellan (2001), *Astrophysical Journal* 563, L183]



**Figure 3.** Coaxial sequence: at  $4 \mu\text{s}$  eight spider legs each go from a gas nozzle on inner 20 cm diameter disk electrode to a gas nozzle on outer annulus electrode. At  $5 - 6.5 \mu\text{s}$  the inner spider legs merge to form a central column. At  $6.5 - 10 \mu\text{s}$  the central column lengthens and so constitutes a jet. At  $10 \mu\text{s}$  the jet starts to kink. [Reprinted figure with permission from S. You, G. S. Yun, and P. M. Bellan, *Physical Review Letters* 95, 045002, 2005, DOI: 10.1103/PhysRevLett.95.045002. Copyright 2005 by the American Physical Society]



**Figure 4.** MHD-driven flows go from both footpoints to middle (apex), pile up both plasma and embedded azimuthal flux, resulting in pinching and increased density. [Reproduced from P. M. Bellan, *Physics of Plasmas* 10, 1999 (2003), DOI: 10.1063/1.1558275 with the permission of AIP Publishing.]



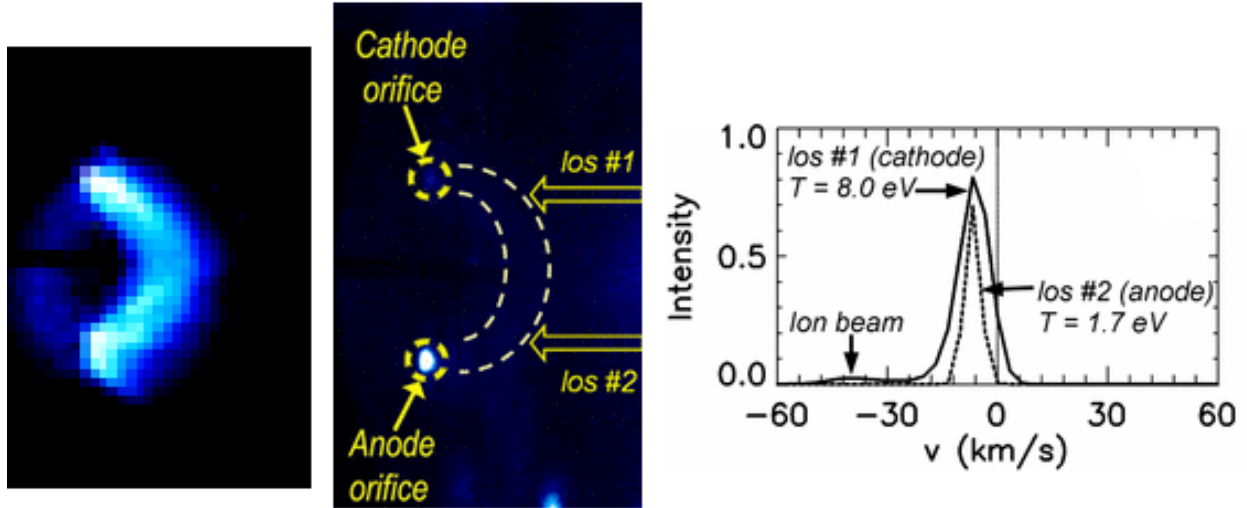


**Figure 6.** Left: photo of experimental replica of solar corona loop at  $t = 1 \mu\text{s}$  after breakdown. Middle: Sketch showing lines of sight (LOS #1, #2) of fiber optic with collimator that goes to spectrometer for measurement at this time. Right: Measured spectra for LOS #1 and LOS#2; coordinate system defined relative to observer so negative velocity is motion towards observer (blueshifted as seen by observer). This figure uses material excerpted with permission from Figs. 1, 4, and 5(a) in *Tripathi et al.* [2007]. Copyright 2007 by the American Physical Society.

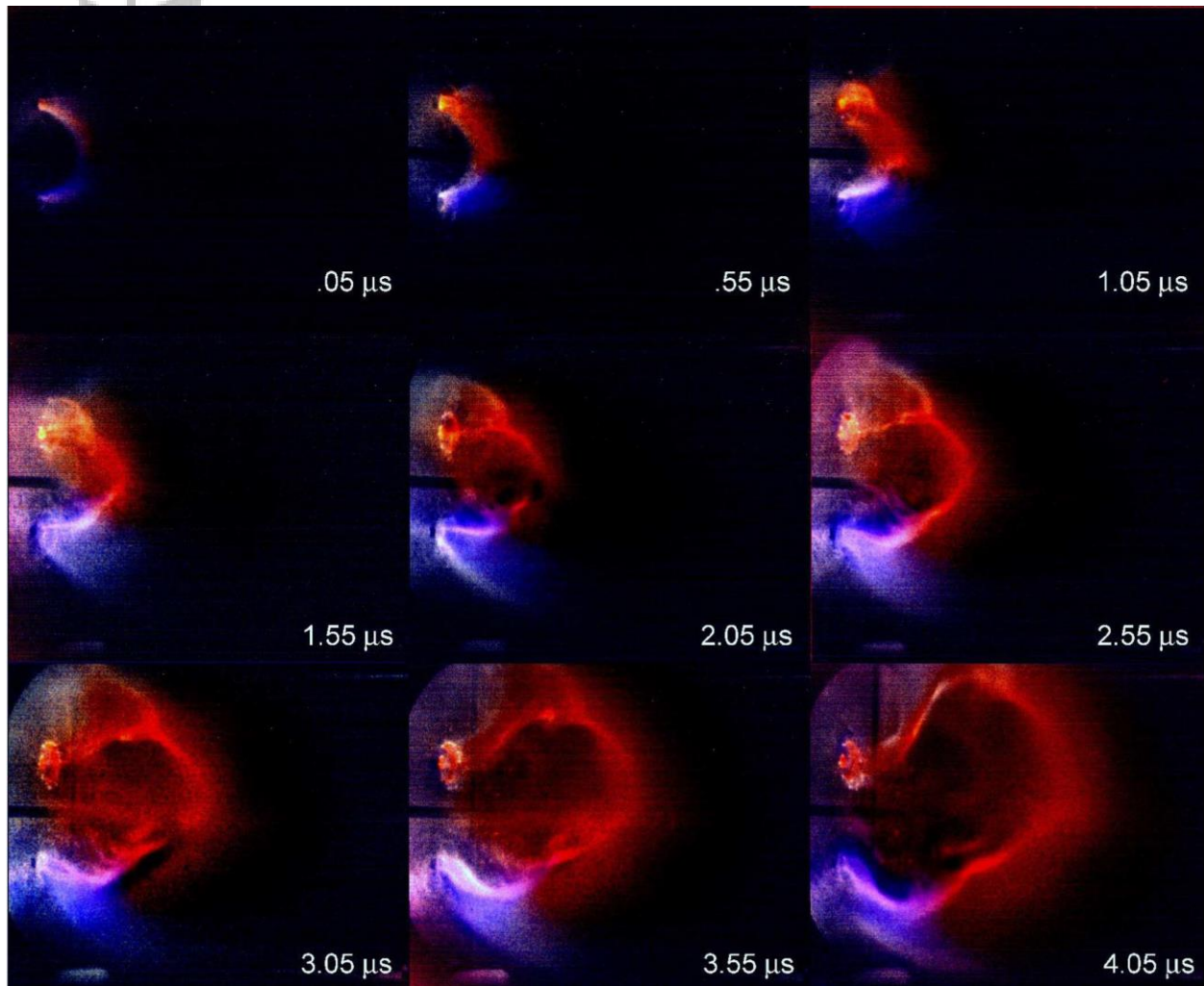


**Figure 7.** Demonstration that gas in loop originates from the footpoints. Hydrogen (red) is injected from top footpoint and nitrogen (purple) is injected from bottom footpoint. The loop consists of a lengthening hydrogen jet butting against a lengthening nitrogen jet. The hydrogen jet is longer because hydrogen, being lighter, is accelerated to higher velocity. The arch major radius increases because of the hoop force (stronger azimuthal magnetic field on concave side than on convex side of arch). © 2008 IEEE. Reprinted, with permission, from IEEE Transactions on Plasma Science 36, 1206, 2008. DOI: 10.1109/TPS.2008.927095

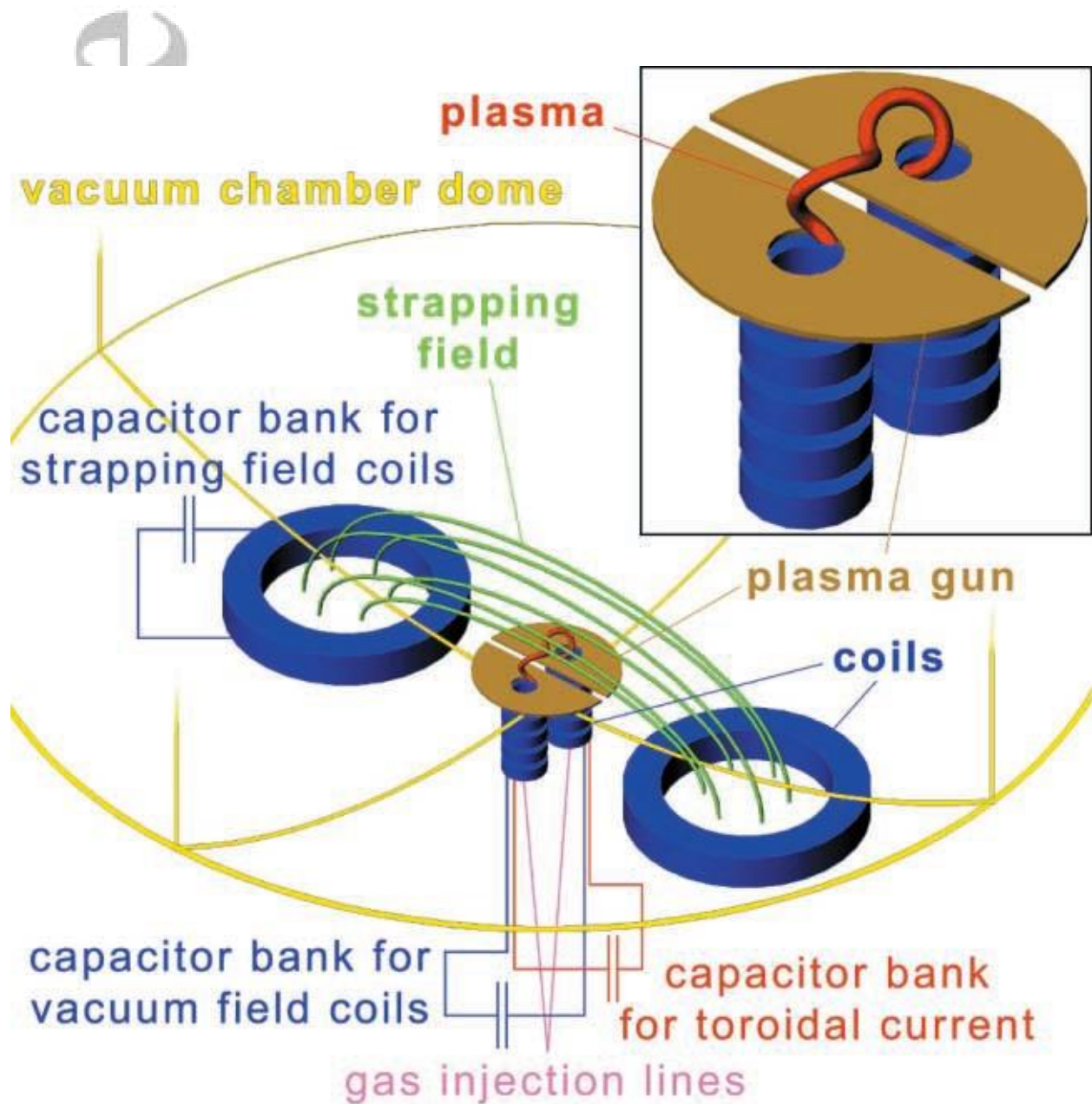


**Figure 8.** Sketch showing strapping magnetic field (green) produced by external coils (blue). [Figure credit: Hansen, J. F., and P. M. Bellan (2001), *Astrophysical Journal* 563, L183]

Accel

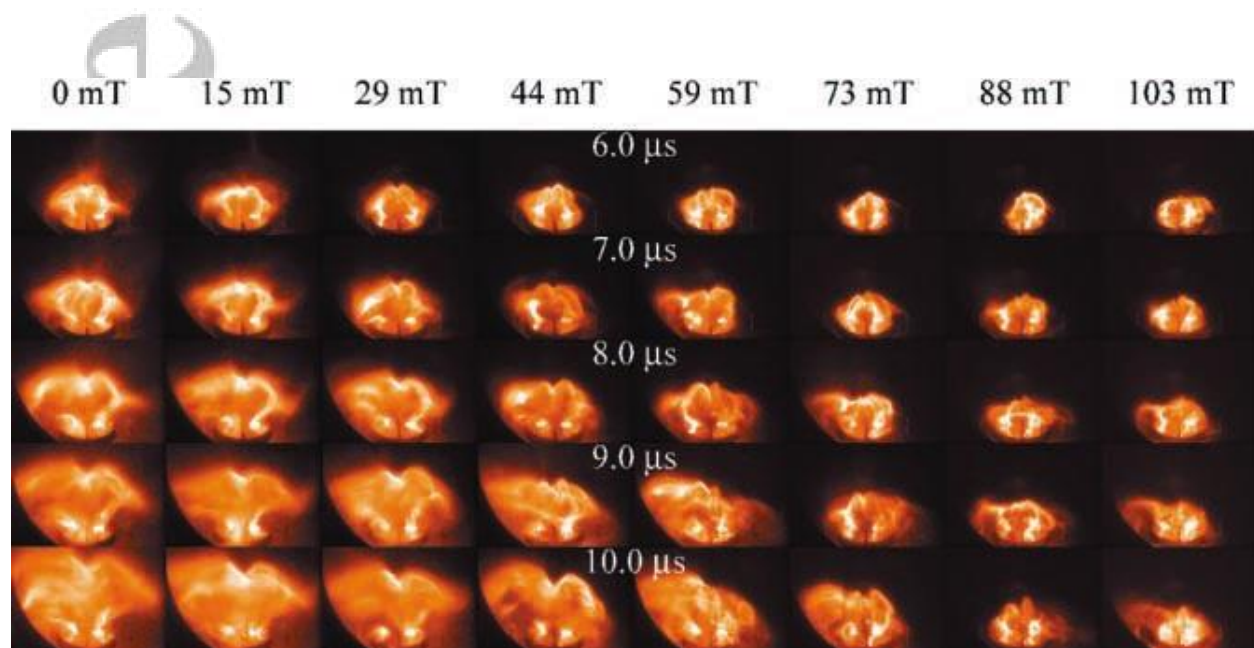


**Figure 9.** Loop expansion versus time for strapping fields ranging from 0 mT to 103 mT. [Figure credit: Hansen, J. F., and P. M. Bellan (2001), *Astrophysical Journal* 563, L183]

Accepted A

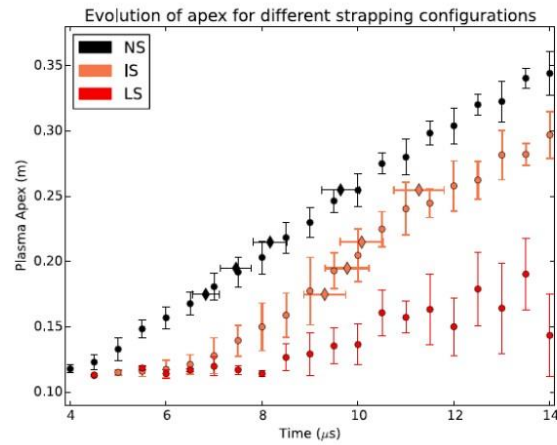
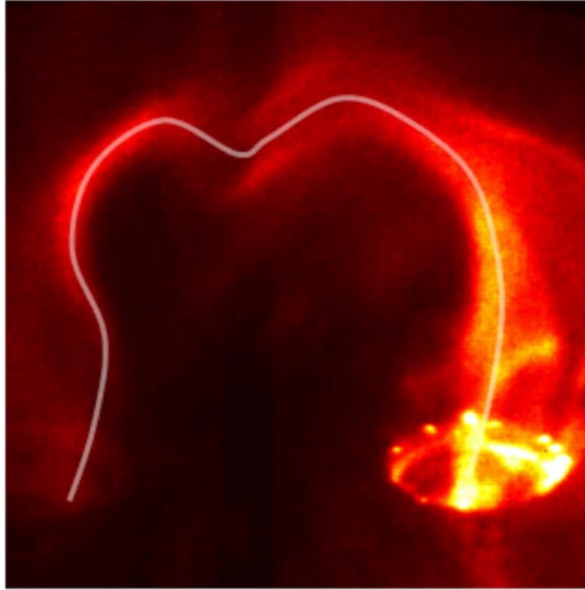
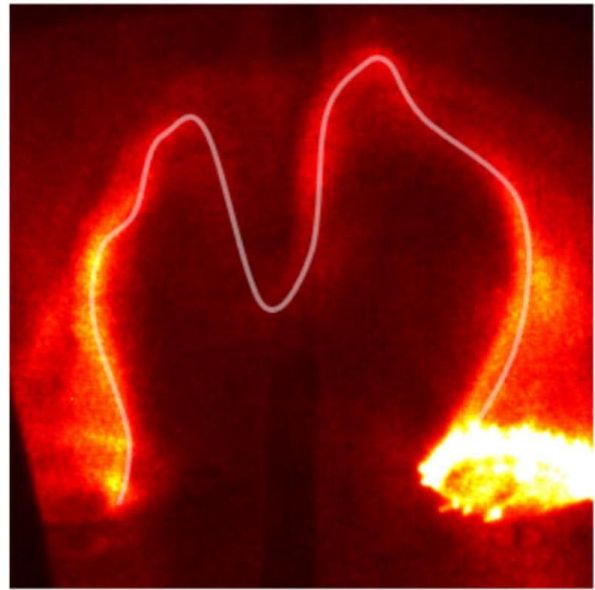


**Figure 10.** With no strapping field (NS) the increase in height of the loop apex is uninhibited. With a large strapping field (LS) the loop is inhibited from expanding. With an intermediate strapping field (IS) the loop is held down at first, but then at about  $6.5 \mu\text{s}$  escapes and accelerates as in the no strapping field case. [Reprinted figure with permission from B. N. Ha and P. M. Bellan, Geophysical Research Letters 43, 9390, 2016, DOI: 10.1002/2016GL069744. Copyright 2016 by John Wiley and Sons]



(a) Smooth dip from low gas density output



(b) Sharp dip from high gas density output

**Figure 11.** Left: Smooth dip from low injected gas density. Right: Sharp dip from high injected gas density. White lines are hand-drawn to indicate axis location. [Figure credit: Wongwaitayakornkul, P., M. A. Haw, H. Li, S. Li, and P. M. Bellan (2017), *Astrophysical Journal* 848, 89]

Accepted

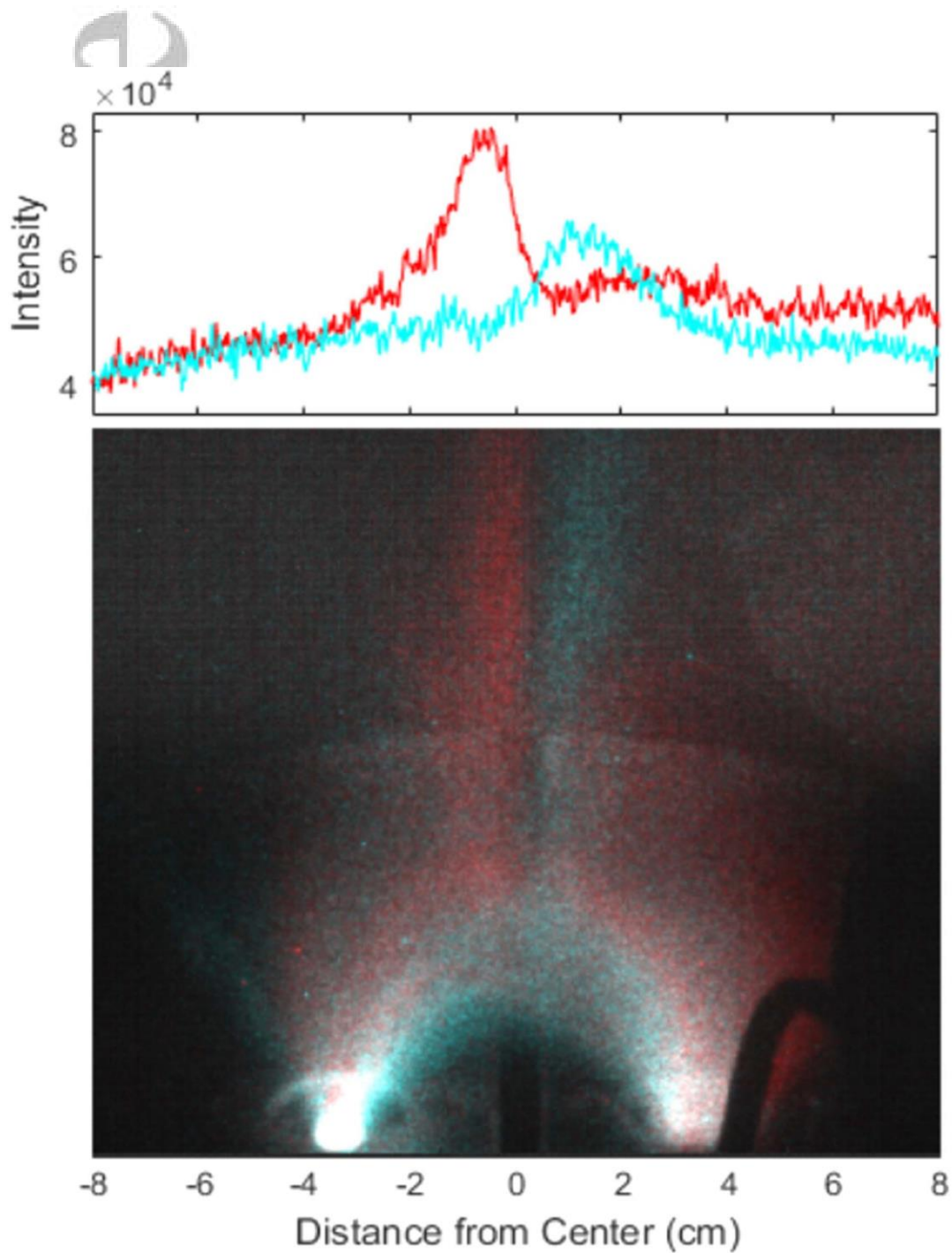
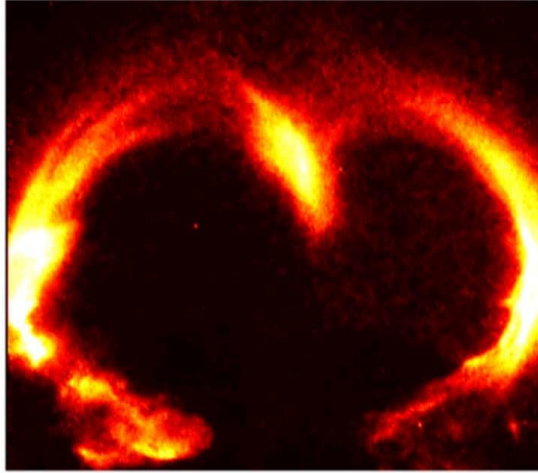


**Figure 12.** Change in location of dip depending on where density maximum is located. Cyan: more higher gas input on right. Red: Higher gas input on left. [Figure credit: Wongwaitayakornkul, P., M. A. Haw, H. Li, S. Li, and P. M. Bellan (2017), *Astrophysical Journal* 848, 89]



(a) Photograph of experimental loop



(b) Synthetic image from simulation

**Figure 13.** Left: Photograph of experimental loop. Right: Synthetic photograph of numerical simulation of loop from 3D MHD code. [Figure credit: Wongwaitayakornkul, P., M. A. Haw, H. Li, S. Li, and P. M. Bellan (2017), *Astrophysical Journal* 848, 89]

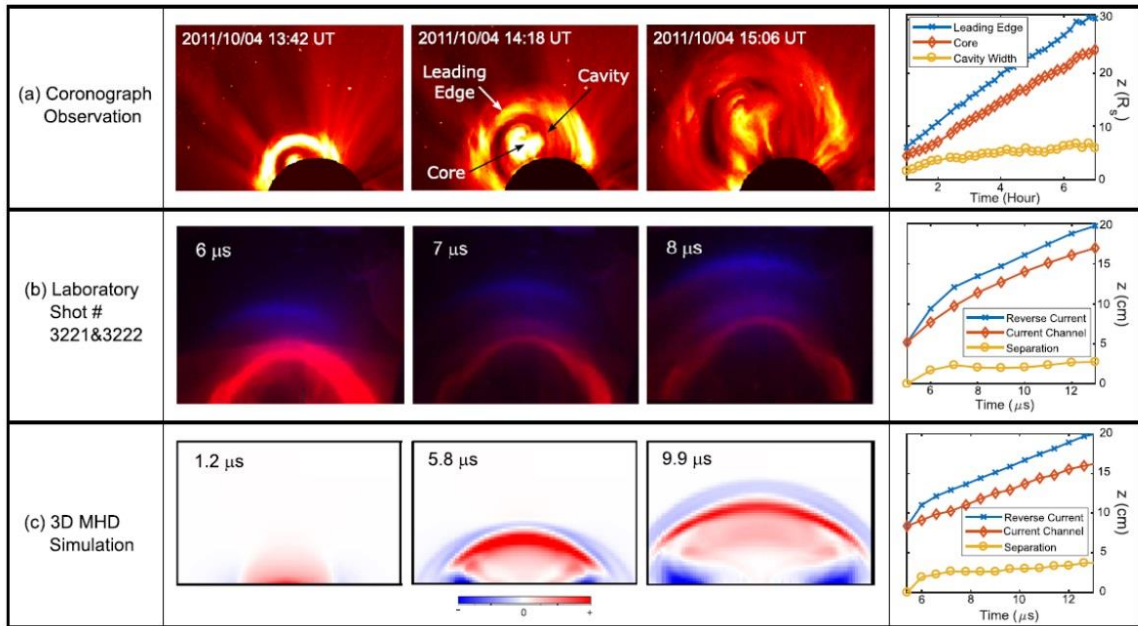


**Figure 14.** (a) Coronal mass ejection observed on Sun. (b) Photos of laboratory experiment showing argon loop (red) expanding into hydrogen background plasma (blue). (c) Numerical simulation from 3D MHD code. [Figure credit: Haw, M. A., P. Wongwaitayakornkul, H. Li, and P. M. Bellan (2018), *Astrophysical Journal*, 862, L15]

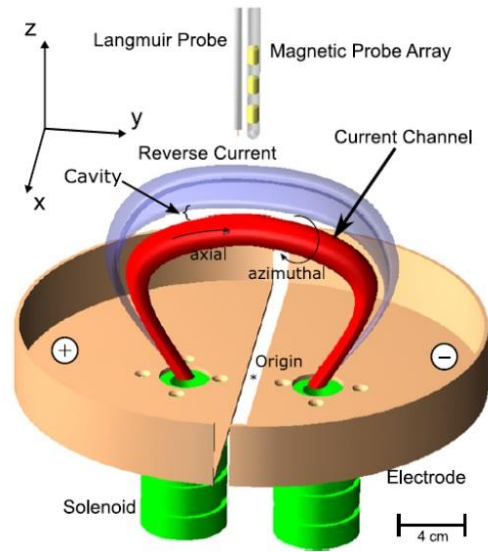


**Figure 15.** Setup of lab plasma showing loop current (red) and induced reverse current (blue). [Figure credit: Haw, M. A., P. Wongwaitayakornkul, H. Li, and P. M. Bellan (2018), *Astrophysical Journal*, 862, L15]

Accepted

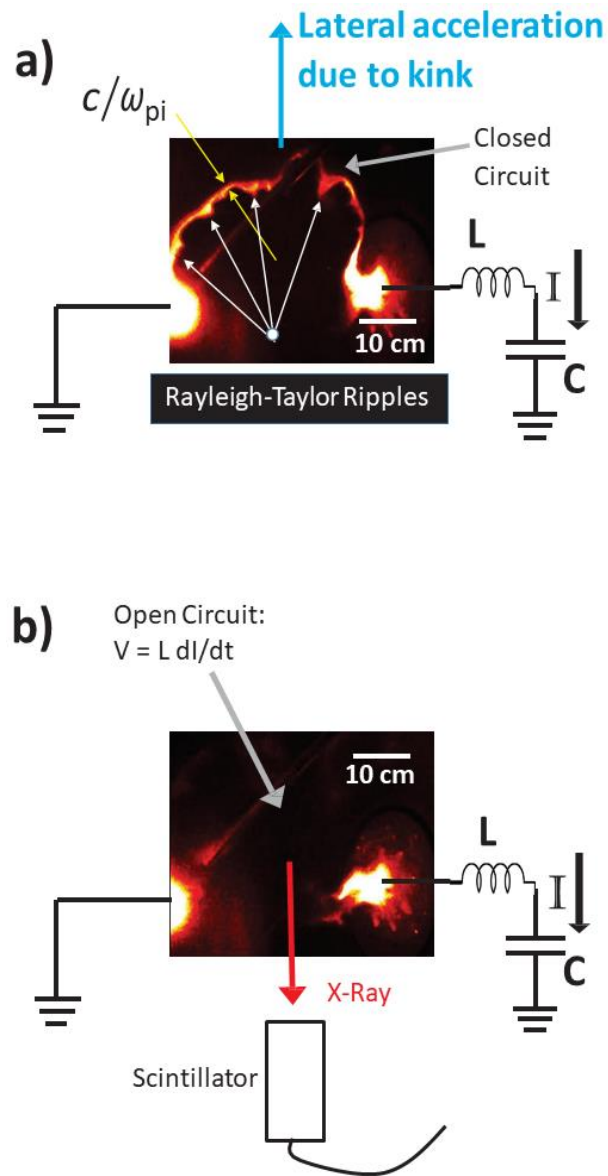


**Figure 16.** (a) Segment of kinked jet; kink is large arch. Small ripples on inboard side are Rayleigh-Taylor instability. Dimming at Rayleigh Taylor instability is evident. The inductance in the rest of the jet circuit and the capacitor bank are sketched as circuit elements. (b) The Rayleigh-Taylor interrupts the current so there is an inductive voltage drop  $V = L di/dt$  that accelerates a small cohort of electrons to energies where they radiate X-rays which are observed by a plastic scintillator. [Reproduced from R. S. Marshall, M. J. Flynn, and P. M. Bellan, *Physics of Plasmas* 25, 112101 (2018), DOI: 10.1063/1.5054927 with the permission of AIP Publishing.]

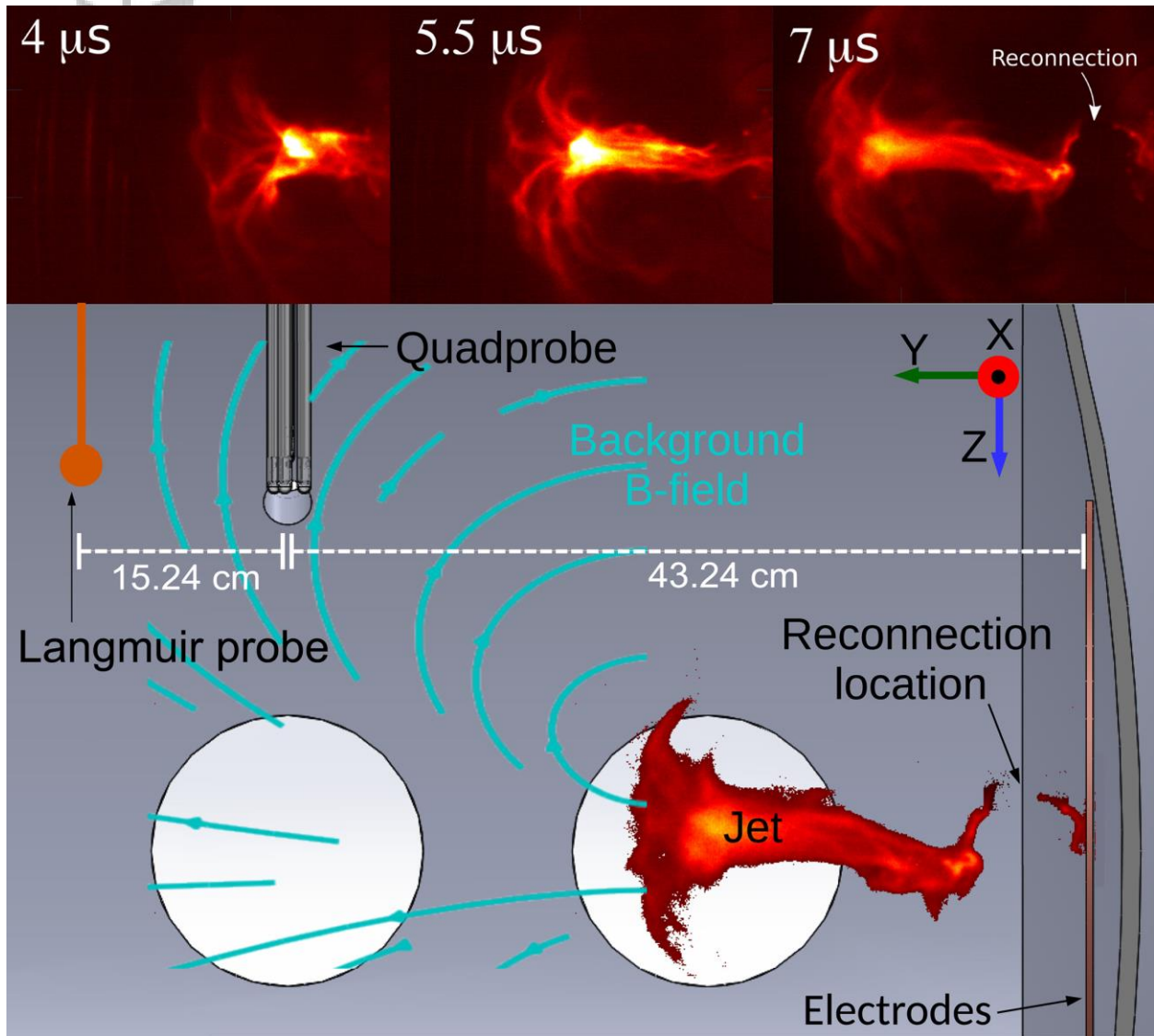


**Figure 17.** Top: time sequence of reconnection. Bottom: location of quadprobe (four-station rf magnetic probe) relative to reconnection region. [Reprinted figure with permission from M. A. Haw, B. Seo, and P. M. Bellan, *Geophysical Research Letters* **46**, 7105, 2019, DOI: 10.1029/2019GL082621. Copyright 2019 by John Wiley and Sons]

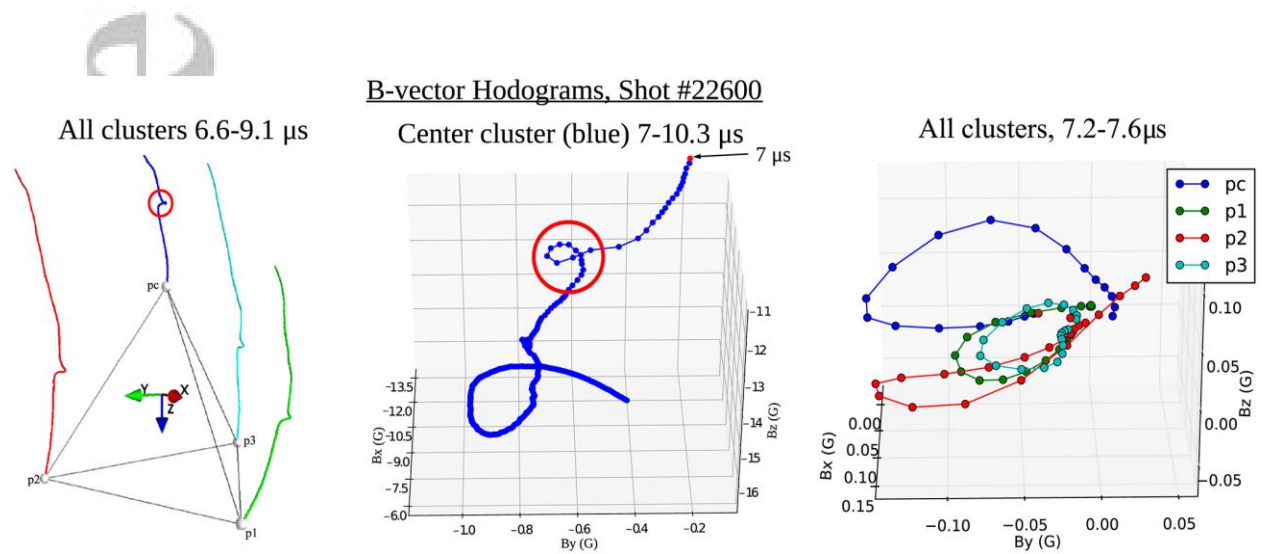


**Figure 18.** Left: signals measured by each of four clusters on quadprobe. Middle: Circular polarization of rf magnetic field as observed by middle cluster. Right: Hodographs of all four clusters. [Reprinted figure with permission from M. A. Haw, B. Seo, and P. M. Bellan, *Geophysical Research Letters* **46**, 7105, 2019, DOI: 10.1029/2019GL082621. Copyright 2019 by John Wiley and Sons]

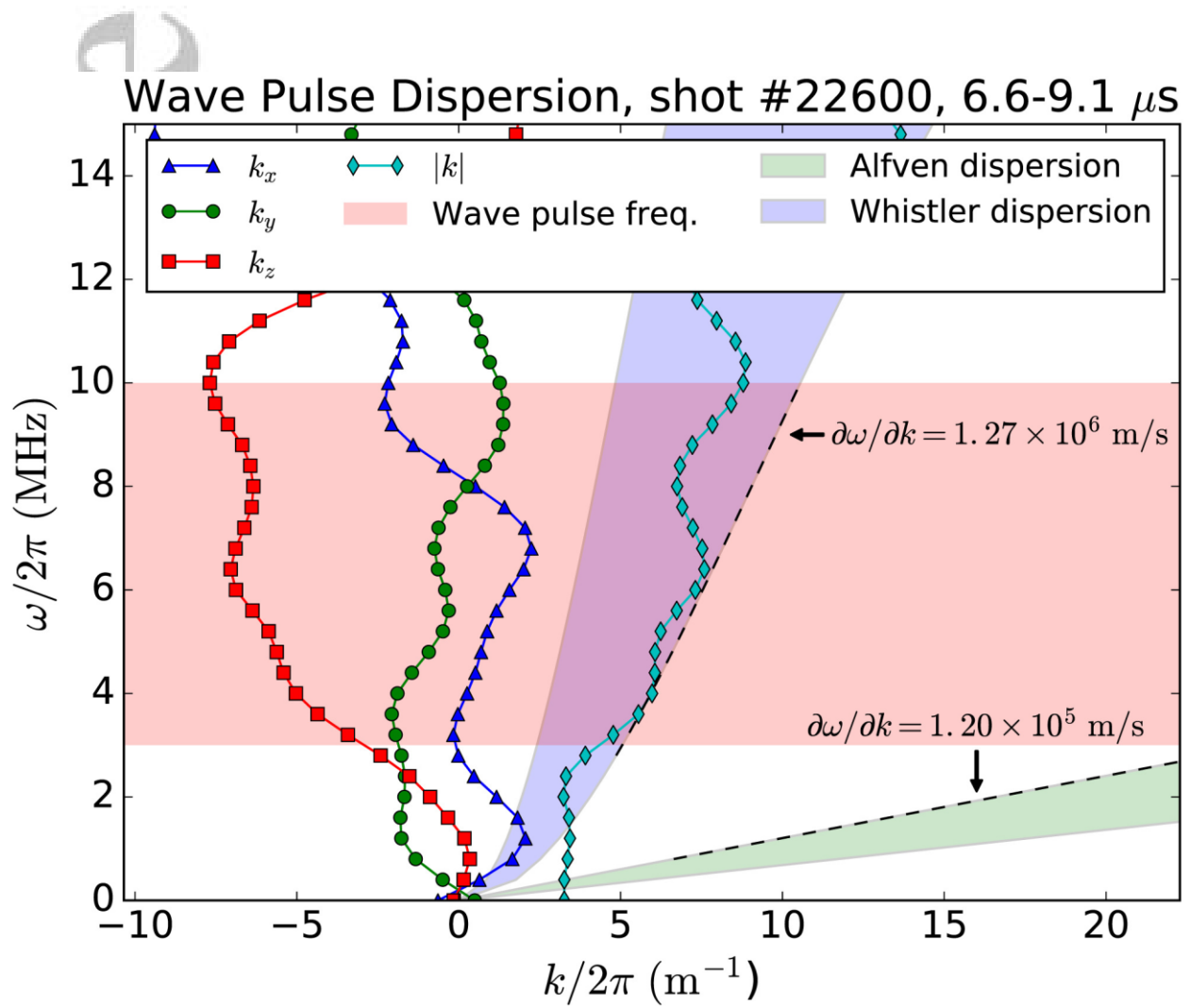


**Figure 19.** Measured dispersion relation is in agreement with whistler wave (purple shaded region) and much faster than Alfvén wave (green shaded region). [Reprinted figure with permission from M. A. Haw, B. Seo, and P. M. Bellan, *Geophysical Research Letters* **46**, 7105, 2019, DOI: 10.1029/2019GL082621. Copyright 2019 by John Wiley and Sons]

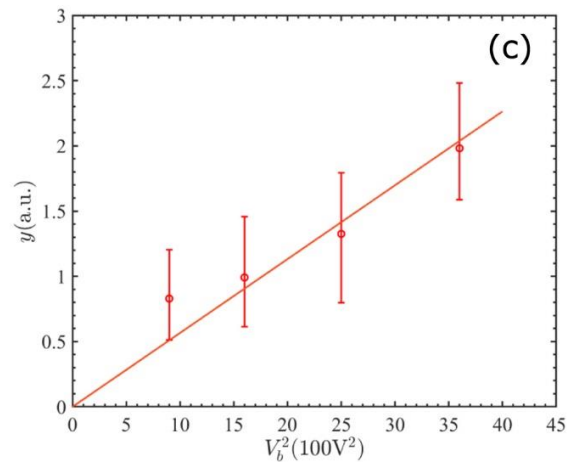
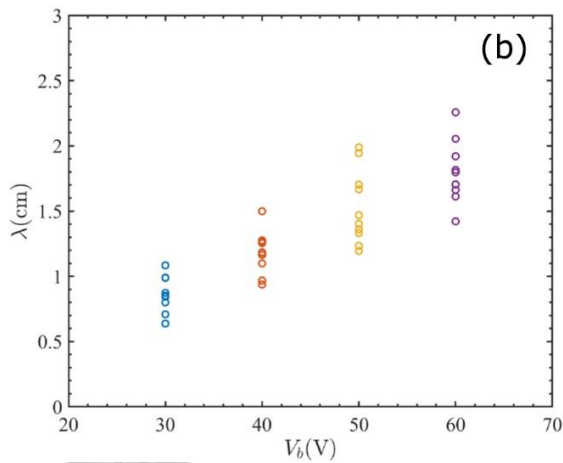
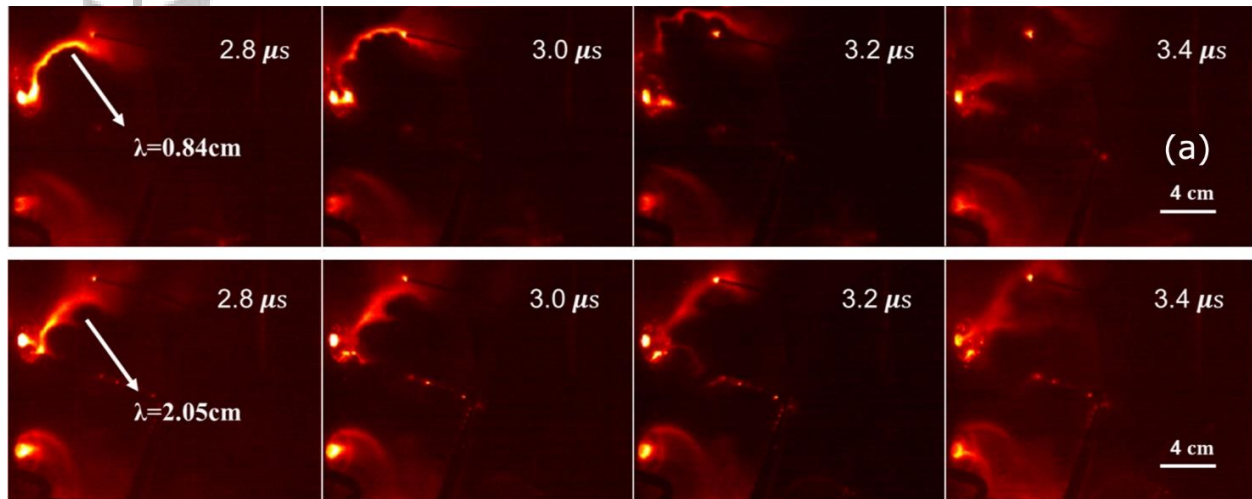


**Figure 20.** (a) Upper row of photos shows Rayleigh-Taylor evolution when bias field is small; lower row shows evolution when bias field is two times larger. Note much longer Rayleigh-Taylor wavelength at  $3.0 \mu s$  in lower row compared to upper row at same time. (b) Scaling of Rayleigh-Taylor wavelength with charge voltage on bias field capacitor (bias field is proportional to this voltage). (c) plot of  $y = \lambda \rho g$  versus square of bias field voltage; compare with Eq.26. [Figure credit: Y. Zhang and P. M. Bellan (2020), *Astrophysical Journal Letters*, 889, L32]